# AN ABSTRACT OF THE THESIS OF

Eric Anderson for the degree of Master of Science in Chemical Engineering presented on November 16, 2009.

Title: Prediction of Mass Transfer Performance of Microchannel Dialyzers using Deconvolution of Impulse-Response Experiments

Abstract approved: _____

Goran N. Jovanovic

The parallel implementation of a large number of functional units is necessary for any industrial scale microfluidic process. The concept of a 'numbering up' strategy where a single highly optimized functional unit that has a low individual production is replicated a large number of times to create a device that has the necessary output. Designing a system using this strategy assumes that the final device will have the performance characteristics of the individual unit. In reality there will be a distribution of operating conditions clustered around the set point, and this will impact the performance of the overall device. The main operating condition of the microfluidic device under consideration here is the average fluid velocity in each channel.

Most techniques that could measure the fluid velocity in each channel require an optical path to the measurement point. For a device with a large number of

channels, it is highly unlikely that every channel will be accessible for observation. Even if they were, it would be extremely time consuming to measure each channel individually. Another approach would be to use an impulse response test to infer the velocity distribution; if an adequately narrow input pulse would yield a output pulse that would be a reasonable approximation of the system response function. In the case at hand, the input pulse is too broad to be able to directly infer the velocity distribution from the output pulse. A numerical deconvolution technique was applied to the data to be able to effectively remove the error associated with the input pulse. For sufficiently accurate impulse response data, this method would yield an accurate estimate of the system response function. Once an estimate of the velocity distribution is known, a method for inferring the performance impact is needed. Two approaches were used: 1. A stochastic simulation that directly generates possible device internal states and then calculates the performance; and 2. A theoretical approach based on the performance surface and and assumed velocity distribution form. Both methods require knowledge of the performance surface of an individual channel with respect to the local velocity. To generate this surface a finite volume was developed in FORTRAN that directly simulates a single microchannel pair. The stochastic model predicted a negative performance impact with increasing velocity distribution variance. A theoretical model was developed that calculates the difference between the real and ideal case using the covariance matrix and Hessian as well as provides a framework for predicting the sign of the deviation in advance.

# Prediction of Mass Transfer Performance of Microchannel Dialyzers using Deconvolution of Impulse-Response Experiments

by

Eric Anderson

A THESIS

submitted to

Oregon State University

in partial fulfillment of
the requirements for the
degree of

Master of Science

Presented November 16, 2009
Commencement June 2010

Master of Science thesis of Eric Anderson presented on November 16, 2009.

APPROVED:

---

Major Professor, representing Chemical Engineering

---

Department Head of the School of Chemical, Biological, and Environmental Engineering

---

Dean of the Graduate School

I understand that my thesis will become part of the permanent collection of Oregon State University libraries. My signature below authorizes release of my thesis to any reader upon request.

---

Eric Anderson, Author

# ACKNOWLEDGEMENTS

This work is the culmination of the efforts of many different people. I would like thank everyone who has helped me through this process. Without your hard work none of this would be possible.

My advisor, Dr.Goran Jovanovic, who not only shaped my graduate experience but is directly responsible for why I am here. His refusal to allow me to change majors as an undergraduate allowed me to find direction in my academic pursuits. His dedication to my education has given me many unique experiences and opportunities.

My graduate committee: Dr. Yokochi, Dr. Paul, and Dr. Fenke. Their valuable insight and patience has made this document possible.

Dr. Kevin Drost, Michael Baker, and Dr. Alex Yokochi; their hard work has allowed me to continue my research for this long. I am thankful for Dr. Yokochi's patience during my initiation into the world of inorganic chemistry.

The Tuhy family for truly treating me like family. I am grateful for their encouragement, advice, and understanding.

My family for their support and patience throughout my education. I can thank my twin brother Aaron for begin there and having a floor to sleep when I needed it. I would like to thank my mom and dad for everything she has done to make my college experience more enjoyable.

I need to thank Alana Warner-Tuhy for her constant support, guidance, and love. She has been my partner in this difficult process, and I know that I could not have done it alone. Her extraordinary ability in the lab is the only reason that I have a single valid data point to work with.

# TABLE OF CONTENTS

# TABLE OF CONTENTS (Continued)

# LIST OF FIGURES

# LIST OF FIGURES (Continued)

# LIST OF APPENDIX FIGURES

# Chapter 1 – Introduction

The miniaturization of chemical processes and unit operations has been an active area of research because of the process intensification that can be achieved by engineering systems with characteristic dimensions of less than one millimeter. Transport processes are more efficient at a smaller length scale because the gradients become very large. Most microfluidic devices can be grouped into two application areas: (1) the production of bulk material and energy, (2) the production of information. Currently, almost all microfluidic and miniaturized devices fall into category two [16].

The problem with applying the principles of microtechnology to bulk material processing is that one micro process unit (MPU) can only process a minuscule amount of material. This is both the strength and the weakness of microtechnology. A MPU can be very highly optimized to most efficiently carry out a operation, but a large number of parallel units will be necessary to process material on the commercial or pilot scale. Many different kinds of microdevices have been been designed and successfully built, ergo the design and construction of a single micro process unit is well within the means of the current state of the art. The technical challenge now is to develop the necessary technologies to 'number up' the micro process units in order to attain the required volume for bulk production.

The numbering up strategy [13], for the scale up of microtechnology based

processes are implicitly based on a fundamental assumption, that an extremely large number of parallel units can be manufactured, and that they will perform identically. The technical challenge of satisfying this requirement may or may not be great, but this is likely dependent on the sensitivity of the individual process unit to errors in manufacturing and conditions. In the case of a microfluidic device that is based on parallel microchannels, the largest deviation in operating conditions from channel to channel will be each channel's velocity. The deviation in channel velocity can be traced to three main causes. The first is a large bubble that completely blocks the flow in one or more channels. The second is a micro-bubble that reduces the local cross-section of the channel, and the third is variance due to manufacturing variation. The first case can be directly detected through a large shift in residence time, which is easily detectable with existing methods. The second and third cases are unlikely to cause a readily detectible shift in residence time or pressure drop, so more sensitive methods of analysis are required to detect these variations.

In the kind of array being analyzed here the decrease in performance of the overall device, when compared to an ideal MPU, will be caused primarily by flow maldistribution within the target device. In this context flow maldistribution will be taken to be a deviation from the intended operating velocity for each channel.

The measurement of flow maldistribution in microfluidic devices has been largely conducted by optical means, usually by the measurement of the velocity of a tracer being carried within the fluid. The problem with this is that in many microfluidic devices, both lab and commercial scale, it is impossible gain access to the channels

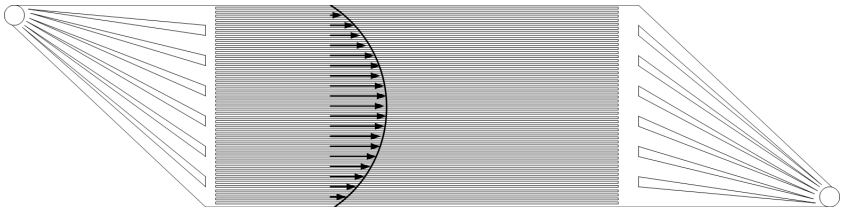

Figure 1.1: Example Flow Distribution in a Microchannel Array

for an optical measurement. An obvious answer to this would be to perform a computational fluid dynamics simulation on the entire device to be able to quantify the local operating point of each channel. While this may be feasible for a lab scale device, present and near future computing capacity will not allow the accurate simulation of a microfluidic device at the bulk production scale. What is needed is a means of characterizing the flow within the device without directly measuring the flow in each channel.

A simpler method for determining the mean residence time in the device is from an impulse response test by injecting a tracer into the inlet of the device and then measuring the output. From this output the mean residence time can be calculated. In order to quantify the impact of flow maldistribution on performance, it is necessary to have more detailed knowledge of the flow field. Much of the information that is contained within the output of the device is lost due to the dispersion of the tracer because of diffusion as well as the imperfect shape of the original impulse. One of the goals of the present work was to develop a method for removing the dispersive and input error in an attempt to recover a closer approximation of the original exit age distribution (E curve) [14].

# Chapter 2 – Stochastic Simulation

## 2.1 Purpose and Methodology

A model to simulate the operational characteristics of a microchanel array will require at least two pieces of information for each channel. The first is that the mean velocity in each channel is known, and the second is that the performance of a microchannel pair will be known for this possible combination of channel-channel velocities. If both of these conditions can be satisfied, then the simulation is strait forward. The fractional removal can then be shown as:

$$F_r = \frac{Q_{in} \cdot C_{in} - Q_{out} \cdot C_{out}}{Q_{in} \cdot C_{in}} \tag{2.1}$$

Where $F_r$ is the fractional removal, $C$ is the concentration, and $Q$ is the total flowrate into the system. For an ideal situation where the channel velocities are known explicitly, the expression above would be exact. For the purposes here the velocities in each channel will not be explicitly known, only the E curve will be known for the device. This stochastic simulation will attempt to determine what is the most probable value of $F_r$. If an accurate approximation of the E curve is known and each microchannel has a steady state velocity field, then the E curve can be used to reconstruct the population of microchannel velocities. Since only the population distribution will be known, then it will not be possible to

uniquely assign a velocity to a given microchannel. It will be possible, however, to reconstruct the extrema values for $F_r$. Since the extrema represent one unique internal device state then these will also be the least likely of the possible states and the most probable state will be bounded by these values. The set of possible internal states would then be:

$$F_r \in \frac{\sum_i uC_{out}A_c}{Q_{in}C_{in}} \tag{2.2}$$

Where the lack of superscript $i$ denotes the non-uniqueness of the velocity and concentration conditions for a given channel.

In order to evaluate the possible fractional removal space, it is necessary to first have a means of approximating each microchannel's local mean velocity. If one were to integrate the E curve from $t$ to $t + \Delta t$ such that it would represent an integer population of microchannels then the average velocity in that set of microchannels could be approximated by the first moment of that slice of the E curve [6].

$$n_{\overline{u}} = \int_t^{t+\Delta t} nE(t)dt \tag{2.3}$$

and

$$\overline{u} \cong \frac{\int_t^{t+\Delta t} nE(t)tdt}{\int_t^{t+\Delta t} nE(t)dt} \tag{2.4}$$

These equations allow for the calculation of the average velocity in a single microchannel in the device. Once this method is applied to the full E curve, then

the approximate population of channel velocities will be known.

At this point the distribution of microchannel velocities is known as well as the surface of possible performances, the combination of which allow for the prediction of microchannel performance based on arbitrary channel-channel velocity pairings. This is all the information that is needed to be able to begin calculating possible internal states.

## 2.2 A Priori Data

This section assumes the knowledge of two important data sets, the performance characteristics of a single micro process unit under arbitrary operating conditions, and the exit age distribution of the fluid. For a microfluidic device, the most obvious means of predicting the performance is a computational fluid dynamics simulation that was in good agreement with known operating points for a well functioning device. This is the method used in the present study. The exit age distribution requires a little more insight into the functioning of the particular device under consideration.

All of the mathematics presented so far assume direct knowledge of the E curve. In the present study the E curve is measured by impulse response experiments, so there is a significant amount of error associated with the original measurement. The differences between the centroid of the input pulse and the exit pulse would ideally be the residence time in a channel, but in actuality there is a significant lag time associated with the headers and the impulse measurement devices themselves.

This, along with the error in the E curve due to the imperfect inlet pulse, is what necessitates a more advanced approach to recovering an accurate representation of the exit age distribution. The approach under consideration here applies deconvolution methods developed for high resolution spectroscopy to remove error from the E curve, where the sources of error can be approximated and successfully removed.

## 2.3 Implementation Details

After the calculation of the E curve and the performance surface for the device is complete, then a means of assigning internal device states for analysis is needed. In this case each microchannel needs to be assigned a mean velocity in such a way that the total population of microchannel velocities matches that of the E curve. In order to satisfy these constraints, it will be necessary to be able to uniquely identify each microchannel in a random manner. The most straightforward way would be to randomly assign a unique random number to each channel. If the channels are then sorted in order from smallest to largest random number, then they can be assigned a mean velocity that fits the distribution, and in effect be 'shuffled' in a way as to create a unique internal state for the device. Then the overall performance metric can be calculated by summing the removal contribution from all of the channels using Equation 3.5.

$$F_r^p = \frac{\sum u^p C_{out}^p A_{ci}}{Q_{in} C_{in}} \tag{2.5}$$

The superscript p denotes a velocity assigned probabilistically according to a known distribution.

If one were to evaluate the above equation for a very large sample size, then the distribution of possible internal states can be found. This distribution should provide both the most probable internal state, and therefore the most probable performance, and a measure of the likely deviation from the expected performance via the variance in the distribution.

## 2.4 Simulation Data

In the absence of accurate experimental data on the microchannel velocity distribution, several test cases were run using the performance surface calculated for a 5.58 cm channel. In order to bring some amount of comparability to standard deviations at different velocities, the index of dispersion was used to generate iso-lines. The index of dispersion is defined as:

$$I_d = \frac{\sigma^2}{\mu} \tag{2.6}$$

Each iso-line corresponds to a constant index of dispersion. So the variance was dependent on the velocity. This can be expressed in a convenient manner by making the variance a fraction of velocity.

$$\sigma^2 = \frac{\mu}{I_d^{-1}} \tag{2.7}$$

The data can be seen in Figure 2.1. Simulation data with a larger index of dispersion could not be accurately obtained due to the error associated with out of bounds interpolation of the performance surface.

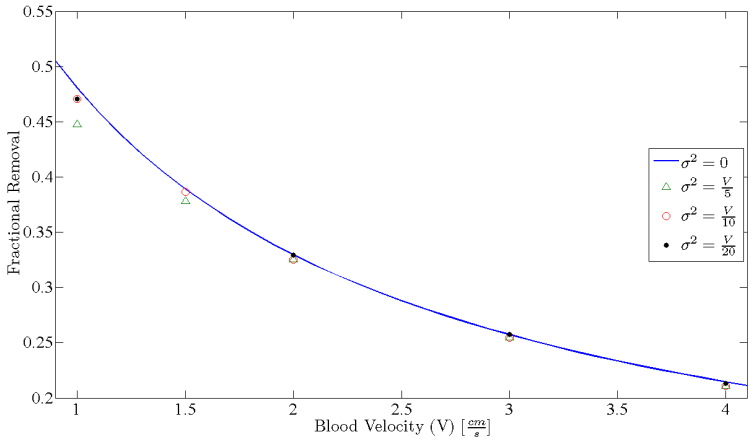


Figure 2.1: Data from the stochastic method compared to the ideal case, $I_d = [0.2, 0.1, 0.05]$

The data points represent the average of 1000 unique internal states which conform to the distribution function. Although individual internal states could have performance values that are slightly higher than the ideal case ($> 1\%$), the averages of the data sets showed a net reduction in fractional removal with respect to the ideal case where variance is equal to zero in most cases. Two cases showed a greater performance, but by less than 0.01%. It is highly likely that this is due to errors in values that are interpolated from the pointwise defined performance surface.. The data suggests that for this particular geometry of the performance surface the decrease in fractional removal is direcly related to the magnitude of the variance.

# Chapter 3 – Finite Volume Simulation

## 3.1 Simulation Goals

The stochastic simulation described for the determination of distribution of internal states of a device assumes an accurate knowledge of the performance characteristics of a single micro process unit. The purpose of the simulation presented here is to accurately predict the mass transfer performance of a single pair of microchannels for a given set of possible flow parameters.

## 3.2 Model Definition

The computational domain consists of two parallel microchannels separated by a porous membrane. The two channels are designed to operate in the counter current flow regime, having equal and opposite magnitude and direction of flow. In practice there will be some error associated with the flow rates into each channel, so the mathematical model will need to be able to include any possible mean channel velocity.

The model was broken into three effective computational domains, the two channels and the membrane. This was done for two reasons. The first is that this cut the memory usage for solving the fluids problem by at least one half including the memory used in preconditioning the problem. The second is that

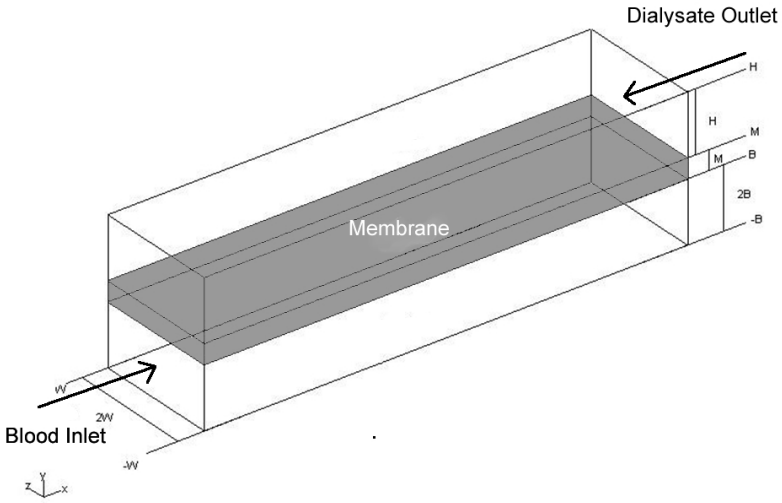


Figure 3.1: Simulation Geometry, Scaled in X

since the pressure correction equation is symmetric and positive definite, preconditioned conjugate gradients is extremely effective at solving this equation set. If the membrane domain were included in the pressure correction equation, then the coefficient matrix would possibly no longer be positive definite and therefore a solver for general equations would be necessary [7]. Of the optimized solvers that were available to the author, all of solvers are Krylov subspace methods, including generalized minimum residual method (GMRES). All of the Krylov subspace methods, with the exception of GMRES, operate on the artificially positive definite coefficient matrix $A^T A$ and therefore the condition number of the equation set is squared. This makes the solution of the equation set more difficult and will result in more stringent precondtioning requirements [3]. GMRES has the disadvan-

tage of having about $150X$ the memory requirements of conjugate gradients and is in general not as effective at solving the SIMPLE pressure correction equation. For these reasons GMRES was used to solve all scalar transport equations, while conjugate gradients was used for the pressure correction equation.

The incompressible Navier-Stokes equations were used to model the fluid mechanics in each microchannel. The equation set in three dimensions [20]:

U Velocity Component

$$\rho(\frac{\partial u}{\partial t} + u\frac{\partial u}{\partial x} + v\frac{\partial u}{\partial y} + w\frac{\partial u}{\partial z}) = \frac{\partial p}{\partial x} + \mu(\frac{\partial^2 u}{\partial x^2} + \frac{\partial^2 u}{\partial y^2} + \frac{\partial^2 u}{\partial z^2}) \tag{3.1}$$

V Velocity Component

$$\rho(\frac{\partial v}{\partial t} + u\frac{\partial v}{\partial x} + v\frac{\partial v}{\partial y} + w\frac{\partial v}{\partial z}) = \frac{\partial p}{\partial y} + \mu(\frac{\partial^2 v}{\partial x^2} + \frac{\partial^2 v}{\partial y^2} + \frac{\partial^2 v}{\partial z^2}) \tag{3.2}$$

W Velocity Component

$$\rho(\frac{\partial w}{\partial t} + u\frac{\partial w}{\partial x} + v\frac{\partial w}{\partial y} + w\frac{\partial w}{\partial z}) = \frac{\partial p}{\partial z} + \mu(\frac{\partial^2 w}{\partial x^2} + \frac{\partial^2 w}{\partial y^2} + \frac{\partial^2 w}{\partial z^2}) \tag{3.3}$$

The boundary conditions were symmetric for each channel. The boundary with the porous membrane was assumed to be continuous in y across both domains.

| Boundary Condition | |
|---|---|
| Inlet | $\mathbf{u} = u_o$ |
| Outlet | $\frac{\partial u}{\partial x} = 0$ |
| Wall | $\mathbf{u} = 0$ |
| Membrane Interface | $v_m = v_c$, continuity |

The transport of fluid within the membrane domain was modeled with Darcy's law. It is assumed that $v_m \gg (u_m, w_m)$ so the membrane velocity can be found by [5]:

$$v_m = H_p \Delta P \tag{3.4}$$

Where $v_m$ is the y velocity in the membrane and $\Delta P$ is the pressure drop across the membrane. $H_p$ is the hyadraulic permeability of the membrane.

Scalar transport is solved throughout the entire computational domain and is modeled with the convection-diffusion equation [21].

$$\nabla(\rho \mathbf{u} \phi) = \nabla(\Gamma \nabla \phi). \tag{3.5}$$

The transport of solute in the membrane uses the effective diffusivity to account for diffusion in porous media. The effective diffusivity, $D_{eff}$, is calculated from literature values for the membrane used in this study [4].

The concentration is defined at each fluid inflow condition, and a convective outflow condition is specified in the fluid outlet.

| Boundary Condition | |
|---|---|
| Blood Inlet | $C = C_o$ |
| Dialysate Inlet | $C = 0$ |
| Outlet | $\frac{\partial C}{\partial x} = 0$ |
| Wall | $D\nabla C - \rho \mathbf{u} C = 0$ |
| Membrane Interface | $C_m = C_c$, continuity |

## 3.3 Details of Finite Volume Implementation

For this simulation the finite volume method was chosen to solve both the computational fluid dynamics problem and the scalar transport problem primarily because of the necessity that the method be conservative. Package finite element method simulations were found to have errors in conservation that were larger than the laboratory error associated with the data that it was to be compared against for reasonably fine mesh.

Since the Reynold's number for the microchannels and flow under consideration is $Re < 10$, then a steady state analysis of device performance is sufficient. The computational domains under consideration have extreme aspect ratios, so it was thought that a pseudo-steady state (PSS) solution might be more efficient than the steady state calculation. Initially the pressure closure scheme implimented was the pressure implicit with splitting of operators (PISO) method. This method has the advantage of being explicit in time, at the expense of solving a second pressure correction equation. After optimizing the simulation it was found

that a PSS solution was not needed and therefore the second pressure correction equation was unnecessary. The semi-implicit method for pressure linked equations (SIMPLE) approach is computationally more efficient with a judiciously chosen under-relaxation parameter for pressure [2].

The other concern was the problem of accuracy, stability, and the memory limitations of the linear algebra solution of very large data sets. The face interpolation method used needed to be of at least second order accuracy to ensure mesh independent results with a reasonably spaced mesh. The Quadratic Upwind Interpolation for Convective Kinetics (QUICK) was implemented because it is third order accurate and easy to implement [18]. Since all high order methods are prone to causing oscillations, or wiggles, in the solution a deferred correction strategy was implemented to render the method unconditionally stable [9].

The implementation of the SIMPLE method involves solving three nonlinear and one linear coupled systems of equations. Picard iteration was implemented to deal with both the nonlinear equations and the equation coupling [7].

$$\text{Solve } A^* x = b \text{ for } x^*$$

$$\text{update coefficients of } A \rightarrow A^*$$

$$\text{check norm of } Ax - b, \text{ terminate if below tolerance}$$

## 3.4 Mesh Dependence Analysis

Even when using a high-order scheme, it is still necessary to determine the mesh dependence of the solution. For the ideal case using QUICK interpolation the error should go down with the cube of the discretized quantity, $\propto O(\Delta\xi)^3$ [18]. Since the mass transfer is heavily dependent on the correct velocity profile, it will take the convergence of all five scalar fields for the mass transfer performance to stabilize. For the purposes of this study, the discretization in both directions orthogonal to the flow, $\Delta y$ and $\Delta z$ were changed and the mass transfer performance recorded.

The final fractional removal was used as the metric for grid dependence. As the mesh is refined , it is assumed that the fractional removal would approach some asymptotic value as $\Delta\xi \rightarrow 0$. The value for the termination of SIMPLE iterations by some threshold value of the pressure correction equation also has an influence on the solution. This is both due to the accuracy of the velocity profile, and therefore the residence time, but also by the accuracy of the convective term of the transport equation in the membrane. The termination value in this code is determined by the relative maximum to the initial maximum of the simple pressure correction equation. This relative pressure correction value, $P'_r$, should be proportional to the error in continuity after the solution of the scalar transport equations for velocity.

$$P'_r = \frac{max(P'_n)}{max(P'_0)} \tag{3.6}$$

Values of the relative pressure correction from $1 \cdot 10^{-1}$ to $1 \cdot 10^{-3}$ were calculated

to determine the necessary level for solution independence. In this simulation it seems that the necessary value of $P_r'$ is mesh dependent, but a value of $1 \cdot 10^{-2}$ is sufficient for solution independence with the grid at the necessary resolution for scalar transport solution.

The necessary level of reduction of $P_r'$ is dependent on the spacial grid refinement. It was found that as the mesh was refined, the necessary level of reduction of the pressure correction values to achieve mesh independence was reduced. This is important because a reasonably preconditioned solver should converge in $\ll (n)$ iterations [21]. The neccessary reduction in pressure correction tolerance necessitates at least $O(n)$ computations per outer iteration. It was found that in order to achieve the minimum accuracy necessary for this study, high grid refinement in the direction normal to the membrane surface is needed.

| Maximum Differential Element | |
|---|---|
| $\Delta x$ | 0.1cm |
| $\Delta y$ | $2.5 \cdot 10^{-4}$cm |
| $\Delta z$ | $1 \cdot 10^{-3}$cm |

# Chapter 4 – Estimation of the Exit Age Distribution

An important characteristic of a flow system is the exit age distribution (E-curve). This is the output response for the system where the impulse response is a dirace $\delta$ function. It describes the residence time that each fluid element experiences in the device. An accurate estimation of the exit age distribution must be known for the population of microchannel mean velocities to be calculated. In order to measure an approximation of the E curve in the lab, a dye is injected into the flow and the output from the device measured. The raw data for such an experiment can be seen below.

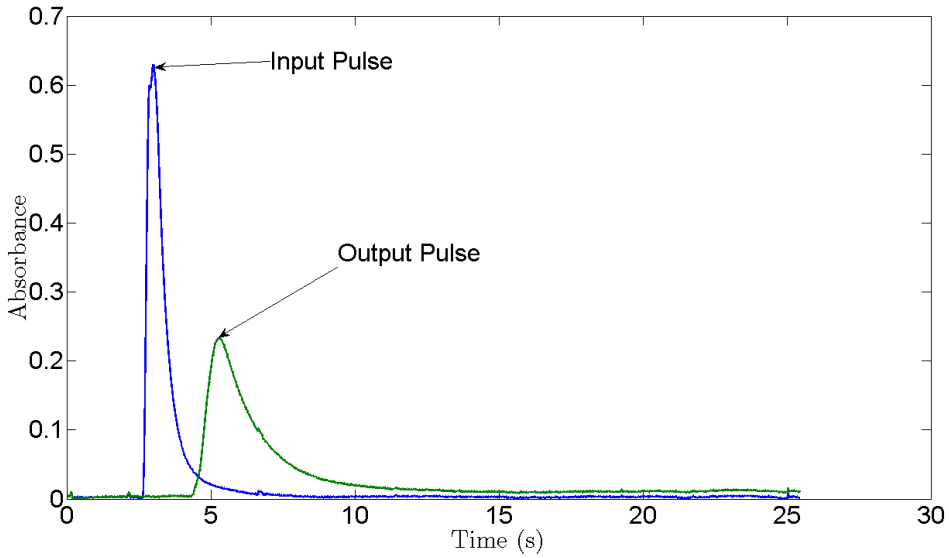


Figure 4.1: Example pulse response data for 0.8 $\frac{ml}{min}$

The output curve from the device contains the information necessary to recover the true E curve, but the measured data is not accurate enough to be used directly [14]. The device output will include the convolution of the E curve and the original pulse shape. For now it will be assumed that the variance of the response function of the laminar microchannel is much smaller than the variance of the original pulse width, $VAR(S_{channel}) \ll VAR(S_{pulse})$. In this case the convolution integral to arrive at the observed output would be [11]:

$$O(t) = \int_{+\infty}^{-\infty} E(t)S(t + d\tau) \tag{4.1}$$

The standard notation for this integral is:

$$E(t) \star S(t) = \int_{+\infty}^{-\infty} E(t)S(t + d\tau) \tag{4.2}$$

This is the definition of the convolution integral. Mathematical methods have been developed to deal with the deconvolution of a response from the system response function. These methods have been used almost exclusively in electrical engineering and spectroscopy [12]. In spectroscopy and most electrical engineering problems, the response function can usually be calculated so the response function is deconvolved with the observed function to give the original impulse. In this case, however, the observed function and the impulse function are known and the system response function is sought.

## 4.1 Deconvolution of Pulse Response Data

In order to be able to derive the system response function for a system of microchannel arrays, it is necessary to have an approximate shape of the impulse in each experiment. When methods for deconvolution are applied to spectrometer data, as most methods have been developed to deal with, the response function is known beforehand. Usually the response function is calculated from quantum mechanical peak broadening due to the excited gas in the spectrometer source. In the case at hand the response function is what is desired, and the input is measured and assumed to be known.

### 4.1.1 Ill-Posedness of the Deconvolution Problem

The discrete case of the convolution integral is the product of the input pulse and the system response function [11].

$$i_n = \sum_{k=1}^{n} o(k)s(k-n) \tag{4.3}$$

From the bounds on the sum then it is obvious that if $s$ were used to generate a symmetric toeplitz matrix then the matrix form of the convolution integral would be:

$$i_n = o_n s_{nn} \tag{4.4}$$

It follows that by the symmetry of the convolution integral then this would be

equivalent to

$$i = s_n o_{nn} \tag{4.5}$$

This sets the basis for solving for the system response function, $s_n$, from known input and observed pulse shapes. The solution of this linear set of equations for $s_n$ would then require the inversion of the toeplitz matrix $o_{nn}$.

$$s_n = i_n o_{nn}^{-1} \tag{4.6}$$

For this reason the deconvolution problem is a general inverse problem. An inverse problem is where the inverse of matrix of experimentally measured coefficients must correlate a known to an observed variable. A general inverse problem is of the form

$$d = G(m) \tag{4.7}$$

Where $G$ is a linear operator that operates on $m$ to find d. In the case of deconvolution the operator $G = s_{nn}^{-1}$, hence being an inverse problem. The problems of stability in solving this linear equation set can be readily seen by the fact that an experimentally measured array of values are highly unlikely to be diagonally dominant or to satisfy the Scarborough criterion.

Inverse problems are, in general, ill posed. The main theoretical limitation (of performing) any true deconvolution is that the solution of the deconvolution operation is not necessarily unique. A perturbation, $\Theta(x)$, whose integral over all

space is vanishing as seen in Equation 5.7

$$\int_{-\infty}^{+\infty} s(x - x')\Theta(x') = 0 \tag{4.8}$$

Will form a valid solution to the convolution integral with the perturbed input function $\Theta(x') + o(x')$ [11].

$$i(x) = \int_{-\infty}^{+\infty} s(x - x')(\Theta(x') + o(x')) \tag{4.9}$$

Another problem relating to deconvolution is that the data will necessarily fail the Scarborough criterion; since the measured set of data points is not diagonally dominant then the toeplitz matrix derived from that data will not be diagonally dominant. This is true even for a judicious choice of data reordering. The maximum value of the outlet pulse was aligned with th first element in all of the simulations conducted. For a an inlet peak of low enough variance it would be possible for the Scarborough criterion to be satisfied, but if this were the case it is unlikely that a deconvolution method would be necessary.

This posses the greatest problem along the baseline of the solution. Since the Central Limit Theorem suggests that the random error associated with the large number of near-zero data points should be a normal Gaussian distribution with an expected value of zero, deconvolution methods are sensitive to error in the baseline of a measurement [11].

As far as solving the linear system of equations, any direct inversion techniques for the topelitz matrix $s$ show an unacceptable amount of baseline error growth.

This generally shows up as synthetic high-frequency peaks in the baseline of the measurement. Mitigation of this effect by low pass filtering has been used [11], but in this study no frequency domain filtering was necessary to stabilize the solution process.

Iterative methods seem to have been the most successful in mitigating baseline error growth and stabilizing the solution, although the toeplitz matrix is ill conditioned for solution by common methods such as Gauss-Seidel or successive over relaxation (SOR) [12]. The matrix $s$ is also not positive definite, so Krylov subspace methods are ineffective at iterative solution of the system of equations. Many methods based on point iterative techniques have been suggested, with varying degrees of success, but most of these methods suffer from physically unrealizable results, which in this case would result in negative concentration. One method, proposed by Jannson et al, uses an approach that not only enforces physical bounds on the solution, but also enforces conservation of area for the curves undergoing deconvolution. This is particularly important for this study as the material balance of the solute is an important metric of the device performance.

### 4.1.2 Jannson's Method

For the purposes of this text the term deconvolution will be defined only as the opposite of *convolution*. The convolution integral is defined as

$$i(x) = \int_{-\infty}^{+\infty} s(x + x')o(x)dx'. \tag{4.10}$$

Where $s(x)$ is the system response function, $o(x)$ is the true impulse response function and $i(x)$ is the observed impulse response function. The discrete vector form of the the convolution integral is the basis for all of the subsequent numerical deconvolution methods and can be seen below:

$$i_n = s_{nn} o_n. \tag{4.11}$$

In the above case $s$ would be a structurally symmetric toeplitz matrix, with each row corresponding to the discrete values of the measured input impulse. For the case of a perfect Gaussian input pulse the matrix would be symmetric, which could be exploited to yield a computational savings during the deconvolution operation. The purpose of deconvolving the imperfect pulse from the input is to gain accuracy in the final approximation of the system response function. General matrix inversion techniques are the obvious first choice to solve this linear system due to the speed and maturity of the algorithms. Due to the high condition number of the toeplitz matrix, the successfull implimentation of direct solvers for normal equation sets is problematic at best [15]. In general, the condition number for the coefficient matrix is at least $10^5$.

Jannson's method is based on the same principle as the SOR method. The method is, in fact, identical to SOR except that the relaxation parameter $\kappa$ is calculated dynamically for each value. As can be seen below the method uses the relaxation parameter $\kappa$ to constrain the iteration to a physically bounded solution.

$$\hat{o}_n^{(k+1)} = \hat{o}_n^{(k)} + \frac{\kappa(\hat{o}_n^{(k)})}{[s]_{nn}} \left( i_n - \sum_{m<n} [s]_{nm} \hat{o}_m^{(k+1)} - \sum_{m \geq n} [s]_{nm} \hat{o}_m^{(k)} \right) \tag{4.12}$$

The relaxation paramater, $\kappa$, is a function of the previous iterate of the system response function. As can be seen in Equation 4.13 $\kappa$ . This forces the next iterate to be within the physical bounds of the simulation, which lends stability to the solver.

The relaxation parameter for Jannson's method requires the beforehand knowledge of the physical limitations of the solution extrema. Since the method was developed for spectrometry, the default range of the function is between zero and one. It is reasonable to assume that a physically realizable system response function will be everywhere positive so the first criterion should be satisfied. As far as the maximum values is concerned, the values of $s(t)$ could become unbounded as long as the area of the response function is one. If Jannson's method for calculating kappa is used, careful attention must be paid to make sure that the response function is not clipped at one by the relaxation parameter.

$$\kappa[\hat{o}_n^k] = \kappa_0 \left( 1 - 2 \left| \hat{o}_n^k - \frac{1}{2} \right| \right) \tag{4.13}$$

Jannson's method was stable for the deconvolution problem at hand. The residual tended to stagnate, but this is likely due to the error inherent in the observed measurement.

As can be seen from the reconstructions of the observed images from the input image and system response function, the solution was a reasonable representation

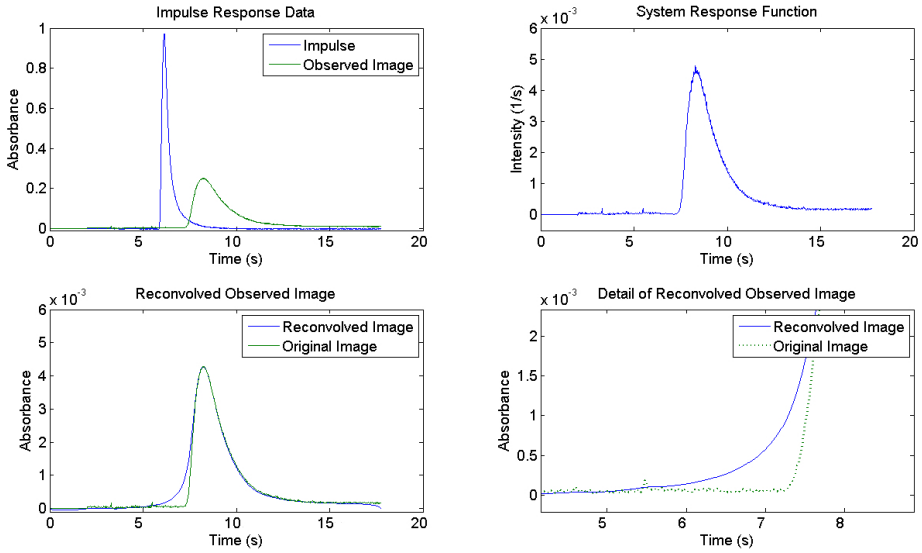


Figure 4.2: Deconvolution Result Using Jannsons Method

of the system response function. The high-derivative region in the begining of the input pulse has been broadened, but this corresponds to the limitations in the time-domain deconvolution model. The rise time of the output curve should be less than the decay time of the inlet curve. Since this is not the case for this data, it causes a slight error in the reconstructed image.

All of the work until this point assumes that the distribution of microchannel velocities is proportional to the system response function. This is true under the condition that the lag time associated with the header is the same for each microchannel. The driving motivation for the design of the header in the device under consideration was the need to keep the total time spent in the header nearly constant for all fluid elements. In order to use this knowledge then it also must be assumed that the center of mass for the system response function represents

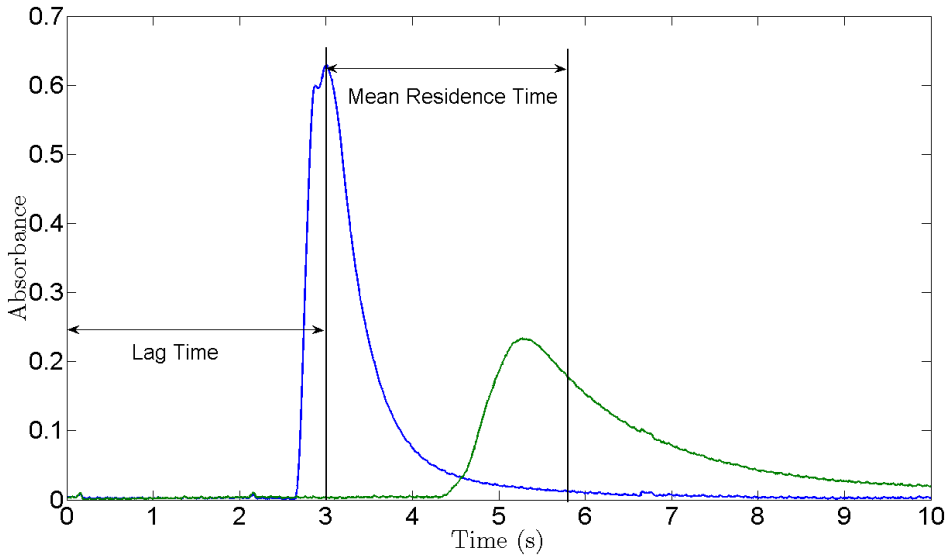


Figure 4.3: Example Impulse Response Test With Labeled Lag Times

the average fluid velocity for all channels. In fact this is a necessary condition for continuity to be satisfied in the device.

To be able to use the reconstructed output data, the difference in the means of the input and the output image have to be about equal to the expected residence time for the device. A small increase in the measured residence time caused by the header and line volumes is unavoidable. This shift is most pronounced at the slowest flowrate, for which the residence time is increased by about 2 seconds. Unfortunately, detailed drawings of the header region are unavaliable, so the expected lag time cannot be computed. The residence time shift was trivial for most of cases described here.

As can be seen from Figure 4.6, the system response function can now be reclassified based on the lag time between the center of mass of the input pulse

and the output image.

$$t_{res} \propto \overline{t_{output}} - \overline{t_{input}} \tag{4.14}$$

Now the system response function can be redefined in time with zero being the center of mass of the input pulse. The x-direction index can then be converted from time to velocity by:

$$v = \frac{L}{t - \overline{t_{input}}} \tag{4.15}$$

The velocity distributions calculated from the data can be found in the appendix.

# Chapter 5 – Sensitivity Analysis of Model Space

The sensitivity of the system to flow maldistribution can be inferred by the shape of the model space, $S(u, v)$. A system whose model space is very highly dependent on flowrate, i.e. $S(u, v)$ has a high curvature, then the system will be more sensitive to flow maldistribution than a system where the model space is nearly flat. There are two extremes that illustrate this point. If the space were everywhere uniform then the performance would be independent of flow so no amount of flow maldistribution would be able to impact device performance. At the other extreme, if $S(u, v)$ is a $\delta$ function at the operating point, then any imperfection in the flow distribution will have a catastrophic impact performance.

To be able to find some relationship between device performance and $S(u, v)$, then a geometrical interpretation of performance is needed. Let's assume that the model space is a two dimmensional continuously differentiable function at the target operating point of the process, say a concave down parabola.

$$y = -x^2 \tag{5.1}$$

If the system were sufficiently optimized to maximize y, then it can be assumed that the operating point is at the point of inflection of the parabola. Now if a perturbation were to be introduced in $x$ so that $x = x_s + x'$ then it is obvious that

$$y_s \geq -(x_x + x')^2 \tag{5.2}$$

That is equivalent to saying that for any perturbation in $x$, the performance of the system will decrease. Conversely, for a concave up parabola, any deviation in x will cause an increase in the effective performance. What is needed is a means of analyzing the local shape of the performance surface to determine the system's local sensitivity to flow maldistribution.

For the subsequent analysis a local operating point must be defined, here denoted with a subscript $s$. That is the point at which the system with no variance in mean channel velocity would be operating, $u_s, v_s$. The performance in $f(u, v)$ would be defined as:

$$f(u, v) = C_o u F_r(u, v) A_c \tag{5.3}$$

This equation would describe the mass being removed from the system per second. This surface is not sufficient since $f(u, v)$ does not take into account the conservative nature of the system. If one channel experiences a positive deviation in velocity, then that means another channel is experiencing a negative deviation in flow to keep the total device flowrate constant. In order to take into account the population of microchannels at a given position $(u, v)$, then $f(u, v)$ needs to be multiplied by the population density distribution $P(u, v)$.

$$S(u, v) = f(u, v) P(u, v) \tag{5.4}$$

It is now necessary to be able to describe the likely distribution of microchannel velocities. If the variations in flow distribution is due to random factors that affect each channel, then it is reasonable to assume that the velocities will be normally distributed around the most probable channel velocity. The bivariate normal distribution is then [8]:

$$P(u,v) = \frac{1}{2\pi\sigma_u\sigma_v} e^{\frac{1}{2\sqrt{1-\rho^2}}(\frac{(u-u_s)^2}{\sigma_u^2}+\frac{(v-v_s)^2}{\sigma_v^2}-\frac{2\rho(u-u_s)(v-v_s)}{\sigma_u sigma_v})} \tag{5.5}$$

Where $\sigma^2$ is the variance with respect to the subscript, and $\rho$ is the correlation coefficient. In the case of an uncorrelated distribution the correlation coefficient will be zero. The population distribution has the property:

$$\iint A_c u P(u,v) du dv = Q_{in} \tag{5.6}$$

In order to be able to evaluate the system with respect to perturbed velocities, $u = u_s + u'$ and $v = v_s + v'$, a second order Taylor Series in two dimensions will be used to approximate the surface [22].

$$\begin{aligned} f(u,v) =& f(u_s,v_s) + (u-u_s)\frac{\partial f(u_s,v_s)}{\partial u} + (v-v_s)\frac{\partial f(u_s,v_s)}{\partial v} + \\ & \frac{1}{2}[(u-u_s)^2\frac{\partial^2 f(u_s,v_s)}{\partial u^2} + 2(u-u_s)(v-v_s)\frac{\partial^2 f(u_s,v_s)}{\partial u \partial v} \\ & (v-v_s)^2\frac{\partial^2 f(u_s,v_s)}{\partial v^2}] \end{aligned} \tag{5.7}$$

So now the surface can be approximated in the vicinity of the operating point.

An algebraic relation is now known for both the distribution function and the probability distribution. The surface $S(u,v)$ can now be calculated:

$$\begin{aligned} S(u,v) =& Af(u_s,v_s)e^{-\frac{1}{2\sqrt{1-\rho^2}}(\frac{x^2}{\sigma_x}+\frac{y^2}{\sigma_y}-\frac{2\rho xy}{\sigma_x\sigma_y})}+ \\ & Ax\frac{\partial f(u_s,v_s)}{\partial u}e^{-\frac{1}{2\sqrt{1-\rho^2}}(\frac{x^2}{\sigma_x}+\frac{y^2}{\sigma_y}-\frac{2\rho xy}{\sigma_x\sigma_y})}+ \\ & Ay\frac{\partial f(u_s,v_s)}{\partial v}e^{-\frac{1}{2\sqrt{1-\rho^2}}(\frac{x^2}{\sigma_x}+\frac{y^2}{\sigma_y}-\frac{2\rho xy}{\sigma_x\sigma_y})}+ \\ & \frac{A}{2}[x^2\frac{\partial^2 f(u_s,v_s)}{\partial u^2}e^{-\frac{1}{2\sqrt{1-\rho^2}}(\frac{x^2}{\sigma_x}+\frac{y^2}{\sigma_y}-\frac{2\rho xy}{\sigma_x\sigma_y})}+ \\ & xy\frac{\partial^2 f(u_s,v_s)}{\partial u\partial v}e^{-\frac{1}{2\sqrt{1-\rho^2}}(\frac{x^2}{\sigma_x}+\frac{y^2}{\sigma_y}-\frac{2\rho xy}{\sigma_x\sigma_y})}+ \\ & y^2\frac{\partial^2 f(u_s,v_s)}{\partial v^2}e^{-\frac{1}{2\sqrt{1-\rho^2}}(\frac{x^2}{\sigma_x}+\frac{y^2}{\sigma_y}-\frac{2\rho xy}{\sigma_x\sigma_y})}] \end{aligned} \tag{5.8}$$

The area under the surface $S(u,v)$ then represents the total transfer of solute from the inlet stream at the given channel population. The volume under this surface is the total transfer of solute for the whole device. This integral is then:

$$\begin{aligned} \iint_{-\infty}^{\infty} S(x,y) = A2\pi\sigma_x\sigma_y\sqrt{1-\rho^2}f(u_s,v_s) + \frac{A}{2}[\pi\sigma_x^3\sigma_y\sqrt{1-\rho^2}\frac{\partial^2 f(u_s,v_s)}{\partial u^2}+ \\ 4\pi\rho\sigma_x^2\sigma_y^2\sqrt{1-\rho^2}\frac{\partial^2 f(u_s,v_s)}{\partial u\partial v} + 2\pi\sigma_x\sigma_y^3\sqrt{1-\rho^2}\frac{\partial^2 f(u_s,v_s)}{\partial v^2}] \end{aligned} \tag{5.9}$$

The full derivation can be found in Appendix A. The integral of $S$ over all space becomes:

$$\mathfrak{S} = f(u_s, v_s) + \frac{1}{2}\left[\sigma_u^2 \frac{\partial^2 f(u_s, v_s)}{\partial u^2} + 2\rho\sigma_u\sigma_v \frac{\partial^2 f(u_s, v_s)}{\partial u \partial v} + \sigma_v^2 \frac{\partial^2 f(u_s, v_s)}{\partial v^2}\right] \quad (5.10)$$

A perfectly functioning system would have a variance for velocity of zero. The difference between this perfectly functioning system and the imperfect system would then be:

$$\mathfrak{D} = \frac{1}{2}\left[\sigma_u^2 \frac{\partial^2 f(u_s, v_s)}{\partial u^2} + 2\rho\sigma_u\sigma_v \frac{\partial^2 f(u_s, v_s)}{\partial u \partial v} + \sigma_v^2 \frac{\partial^2 f(u_s, v_s)}{\partial v^2}\right] \quad (5.11)$$

The deviation function, $\mathfrak{D}$, can be be further simplified. The covariance matrix, $\mathbf{\Sigma}$, for a bivariate distribution is [22]:

$$\mathbf{\Sigma} = \begin{bmatrix} \sigma_x^2 & \rho\sigma_x\sigma_y \\ \rho\sigma_x\sigma_y & \sigma_y^2 \end{bmatrix} \quad (5.12)$$

The Hessian, $H$, for the original Taylor expansion is also needed [17].

$$H = \begin{bmatrix} \frac{\partial^2 f(u_s, v_s)}{\partial u^2} & \frac{\partial^2 f(u_s, v_s)}{\partial u \partial v} \\ \frac{\partial^2 f(u_s, v_s)}{\partial u \partial v} & \frac{\partial^2 f(u_s, v_s)}{\partial v^2} \end{bmatrix} \quad (5.13)$$

Assuming that $f(u_s, v_s)$ is continuous, then the Hessian is symmetric and the Schur Product of the covariance matrix and the Hessian is:

$$Sh = \mathbf{\Sigma} \cdot H = \begin{bmatrix} \sigma_x^2 \frac{\partial^2 f(u_s,v_s)}{\partial u^2} & \rho\sigma_x\sigma_y \frac{\partial^2 f(u_s,v_s)}{\partial u \partial v} \\ \sigma_x\sigma_y \frac{\partial^2 f(u_s,v_s)}{\partial u \partial v} & \sigma_v^2 \frac{\partial^2 f(u_s,v_s)}{\partial v^2} \end{bmatrix} \tag{5.14}$$

The deviation function can then be described by:

$$\mathfrak{D} = \frac{1}{2}\Sigma\left(H \cdot \ \mathbf{\Sigma}\right) \tag{5.15}$$

## 5.1 Geometric Interpretation of Sensitivity

To be able to draw broad conclusions about the performance impact of flow maldistribution on performance, it is necessary to take a closer look at the shape of the deviation space. The performance space is:

$$\begin{aligned} S(u,v) =& Af(u_s,v_s)e^{-\frac{1}{2\sqrt{1-\rho^2}}(\frac{x^2}{\sigma_x}+\frac{y^2}{\sigma_y}-\frac{2\rho xy}{\sigma_x\sigma_y})} + \\ & Ax\frac{\partial f(u_s,v_s)}{\partial u}e^{-\frac{1}{2\sqrt{1-\rho^2}}(\frac{x^2}{\sigma_x}+\frac{y^2}{\sigma_y}-\frac{2\rho xy}{\sigma_x\sigma_y})} + \\ & Ay\frac{\partial f(u_s,v_s)}{\partial v}e^{-\frac{1}{2\sqrt{1-\rho^2}}(\frac{x^2}{\sigma_x}+\frac{y^2}{\sigma_y}-\frac{2\rho xy}{\sigma_x\sigma_y})} + \\ & \frac{A}{2}[x^2\frac{\partial^2 f(u_s,v_s)}{\partial u^2}e^{-\frac{1}{2\sqrt{1-\rho^2}}(\frac{x^2}{\sigma_x}+\frac{y^2}{\sigma_y}-\frac{2\rho xy}{\sigma_x\sigma_y})} + \\ & xy\frac{\partial^2 f(u_s,v_s)}{\partial u\partial v}e^{-\frac{1}{2\sqrt{1-\rho^2}}(\frac{x^2}{\sigma_x}+\frac{y^2}{\sigma_y}-\frac{2\rho xy}{\sigma_x\sigma_y})} + \\ & y^2\frac{\partial^2 f(u_s,v_s)}{\partial v^2}e^{-\frac{1}{2\sqrt{1-\rho^2}}(\frac{x^2}{\sigma_x}+\frac{y^2}{\sigma_y}-\frac{2\rho xy}{\sigma_x\sigma_y})}] \end{aligned} \tag{5.16}$$

Now to characterize the resulting surface the Jacobian and Hessian matrices at the operating point are needed. The Jacobian evaluated at the operating point is:

$$J = \begin{bmatrix} 0 & 0 \\ 0 & 0 \end{bmatrix} \tag{5.17}$$

Since the first derivative is zero at the operating point, then it must be a maximum or minimum. The concavity of the surface can be determined by calculating the eigenvalues of the Hessian matrix. The Hessian for this system is:

$$H = \begin{bmatrix} A\frac{\partial^2 f(u_s,v_s)}{\partial u^2} & A\frac{\partial^2 f(u_s,v_s)}{\partial u \partial v} \\ A\frac{\partial^2 f(u_s,v_s)}{\partial u \partial v} & A\frac{\partial^2 f(u_s,v_s)}{\partial v^2} \end{bmatrix} \tag{5.18}$$

The eigenvalues can be calculated by the characteristic equation [1]:

$$H = \begin{vmatrix} \frac{\partial^2 f(u_s,v_s)}{\partial u^2} - \lambda & \frac{\partial^2 f(u_s,v_s)}{\partial u \partial v} \\ \frac{\partial^2 f(u_s,v_s)}{\partial u \partial v} & \frac{\partial^2 f(u_s,v_s)}{\partial v^2} - \lambda \end{vmatrix} \tag{5.19}$$

So the characteristic equation becomes:

$$\begin{aligned} &\lambda^2 - \left(\frac{\partial^2 f(u_s,v_s)}{\partial u^2} + \frac{\partial^2 f(u_s,v_s)}{\partial v^2}\right)\lambda + \\ &\left(\frac{\partial^2 f(u_s,v_s)}{\partial u^2}\frac{\partial^2 f(u_s,v_s)}{\partial v^2} - \left(\frac{\partial^2 f(u_s,v_s)}{\partial u \partial v}\right)\right) = 0 \end{aligned} \tag{5.20}$$

Combine variables to simplify.

$$det(H) = \left( \frac{\partial^2 f(u_s, v_s)}{\partial u^2} \frac{\partial^2 f(u_s, v_s)}{\partial v^2} - \left( \frac{\partial^2 f(u_s, v_s)}{\partial u \partial v} \right) \right) \tag{5.21}$$

$$C = \left( \frac{\partial^2 f(u_s, v_s)}{\partial u^2} + \frac{\partial^2 f(u_s, v_s)}{\partial v^2} \right) \tag{5.22}$$

$$\tag{5.23}$$

Which simplifies the characteristic equation to:

$$\lambda^2 - C\lambda + det(H) = 0 \tag{5.24}$$

Solving for eigenvalue cases [1]:

$$\begin{array}{lll} det(H) > 0 & \frac{\partial^2 f(u_s, v_s)}{\partial u^2} > 0 & \text{positive definite} \\ det(H) > 0 & \frac{\partial^2 f(u_s, v_s)}{\partial u^2} < 0 & \text{negative definite} \\ det(H) < 0 & & \text{saddle point} \\ det(H) = 0 & & \text{indeterminate} \end{array} \tag{5.25}$$

If the determinant of the Hessian is zero then the point is degenerate and the eigenvalues have only the trivial result. The only way that the determinant could be negative is to have mixed signs on the on-diagonal terms. If the surface in question is negative definite, then flow maldistribution will have a uniformly detrimental impact on performance. If the matrix is positive definite then the flow maldistribution will cause an increase in performance. In the case of a negative determinant, the deviation depends on the magnitude of the on-diagonal elements

as well as the variance in the orthogonal direction.

## 5.2 Comparison with Ideal Model Results

The deviation function relates the error associated with flow maldistribution with the ideal case. A comparison between the corrected fractional removals and the ideal case can be seen in Figure 5.1.

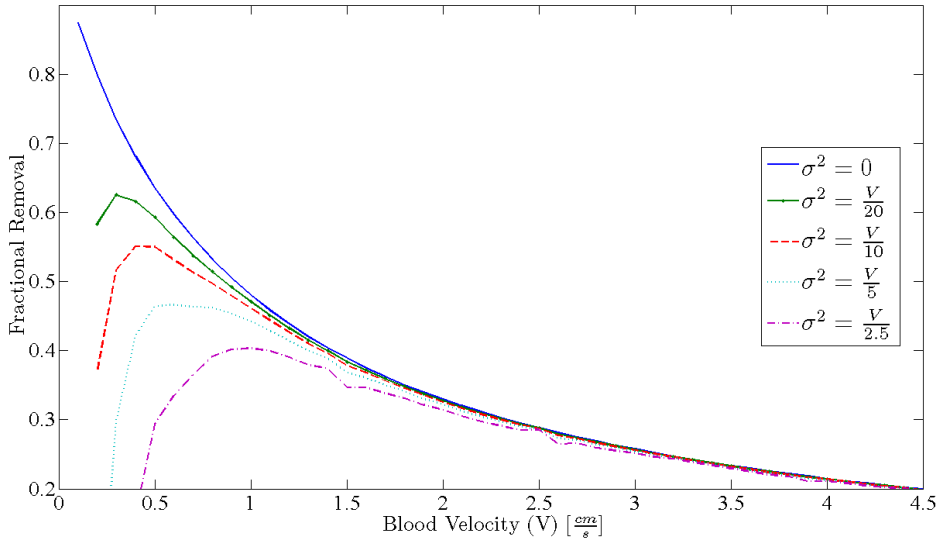


Figure 5.1: Fractional Removal Comparison, $\sigma^2 = 0 \rightarrow \frac{v}{2.5}$

It can be seen that as the velocity approaches zero and the system becomes more nonlinear, the effect of flow maldistribution becomes more pronounced. A comparison graph with bounds representing the operating range of experimental data can be seen in Figure 5.2. For all but the most extreme cases, the deviation would be hard to detect through comparison of experimental data with model

results. Since the blood velocity cannot safely be less than 1 $\frac{cm}{s}$ then the extrema are not important for the present study.

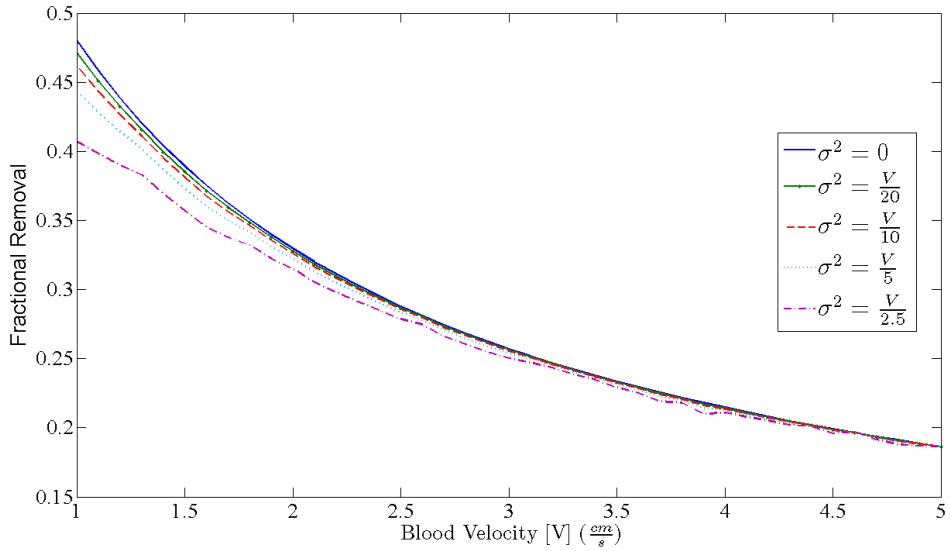


Figure 5.2: Fractional Removal Comparison Within the Operating Range

The 'wiggles' in the corrected fractional removal iso-lines is due to instability in the numeric differentiation of the performance surface. The surface was evaluated using central differencing of $O(h^4)$. This decreased the numerical noise significantly from second order central differencing. For fourth order central differencing:

$$f''(x_0) = \frac{-f_2 + 16f_1 - 30f_0 + 16f_{-1} - f_{-2}}{12h^2} \tag{5.26}$$

## 5.3 Comparison Between Stochastic and Analytic Solution

A parametric study of fractional removal with respect to blood channel velocity and index of dispersion was conducted from both the analytical and stochastic framework. Both approaches were based on the performance surface generated by the finite volume simulation of a 5.58 cm channel. The data for $\sigma^2 = \frac{v}{5}$ can be seen in figure 5.3. The two methods predict nearly identical fractional removal decreases for the non ideal case.

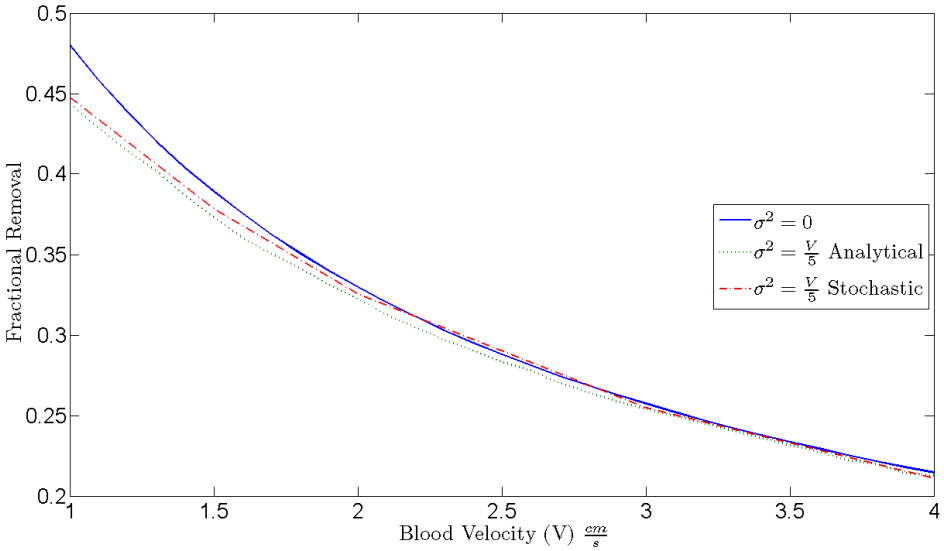


Figure 5.3: Comparison of the decrease in fractional removal with $\sigma^2 = \frac{v}{5}$ for Stochastic and Analytic Approaches

Figure 5.3 represents the largest variance as well as the largest deviation from the ideal. In Figure 5.4, a simulations with a variance of $\frac{v}{10}$ is presented.

As in the previous example, there is good agreement between the analytic and stochastic methods. Both predict a decrease in fractional removal that is

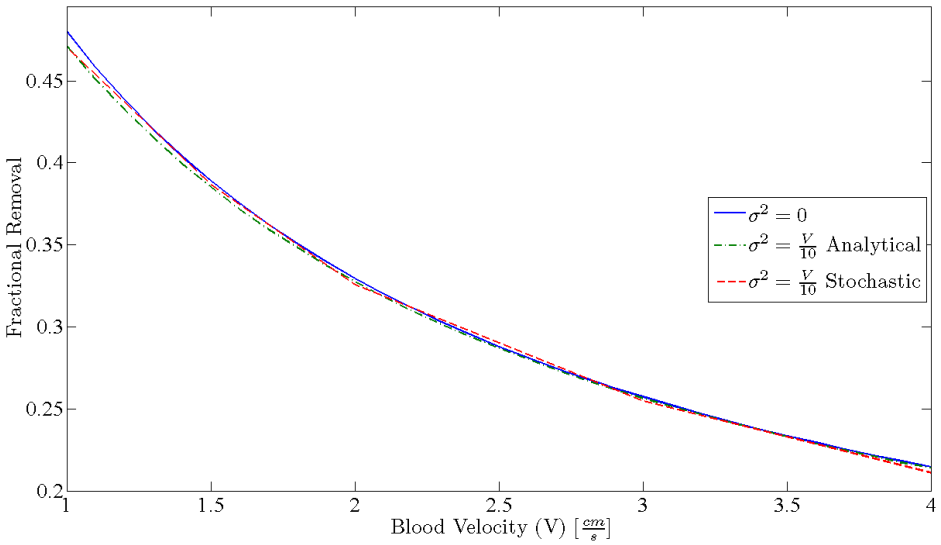


Figure 5.4: Comparison of fracional removal reduction data for $\sigma^2 = \frac{v}{10}$

proportional to variance. A detailed plot of this comparison can be seen in Figure 5.5.

Since both methods give comparable results, then no method is obviously superior to the other. For a case where the performance surface is known to be monotonic, then the analytic method requires far less information about the performance surface than the stochastic method does. On the other hand, if the surface has either local extrema or a distribution that is much larger than the characteristic curvature of the surface then the analytic approach loses validity and a stochastic simulation is necessary.

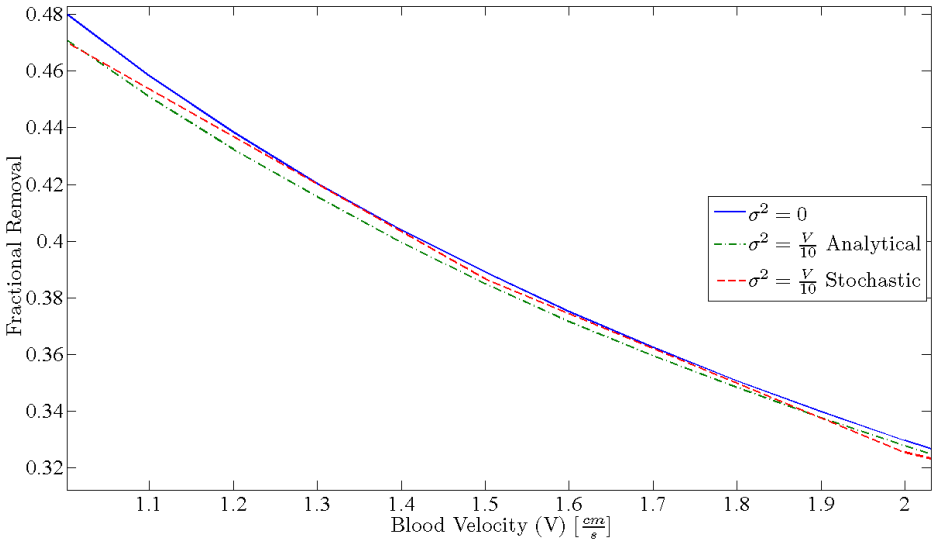


Figure 5.5: Closup of fractional removal comparison for $\sigma^2 = \frac{v}{10}$

# Chapter 6 – Materials and Methods

## 6.1 Mass Transfer Data

The mass transfer data used to compare model results in this paper are mostly taken from Alana Tuhy's thesis, so the interested reader should refer to [19]. A section on the methods used to collect this data is included here is to give the reader a basis for understanding how to compare the experimental data with the experimental work done here.

The microchannel device for which the mass transfer results of the simulation are compared against has the following characteristics.

| Device Parameters | |
|---|---|
| Channel Length (cm) | 5.58 |
| Channel Depth ($\mu m$) | 100 |
| Channel Width ($\mu m$) | 200 |

And the membrane characteristics.

| AN69 Membrane | |
|---|---|
| Thickness ($\mu m$) | 20 |
| Material | acetonitrile |
| Manufacturer | Gambro |

This device and membrane combonation was used to test several solutes, not all of which are included in this paper. Urea was chosen as the solute for this paper since it's diffusivities in water and the effective diffusivity in water are well known. The exact data collection protocol can be found in [19], so the details of device assembly and membrane preparation will be skipped. The preparation was conducted so that there were no residual contaminants in the membrane and the device was sealed with the lowest possible amount of force.

The experiment was conducted as follows. First, a solution of known concentration of solute was prepared using deionized water and reagent grade solute. This solution was then pumped at constant volumetric flowrate through one side of the device. On the opposing side an equal flowrate of deionized water was pumped in counter flow configuration. The system was allowed to reach steady state and then a sample was collected. The collection time and mass collected was recorded for each sample. A commercial spectrophotometric test was used to determine the solute concentrations in both outlet streams. In order for the data to be considered accurate the material balance of the entire system had to be less than two percent.

## 6.2 Pulse Test Experiments

The experimental determination of the exit age distribution curve was carried out by injecting a pulse of known shape into the inlet flow into the microchannel array. By measuring the output it will be possible to infer the true E curve. Both the inlet and the exit pulses were measured to ensure that a perceived flow irregularity

was not in fact merely a misshapen inlet pulse. The injector [Valco] is of the type used to for the injection systems in high pressure liquid chromatography (HPLC). It is necessary for the analyte pulse in the inlet of the chromatographic column be of narrow variance to be able to resolve the eluted peaks. A diagram of the apparatus can be seen below.

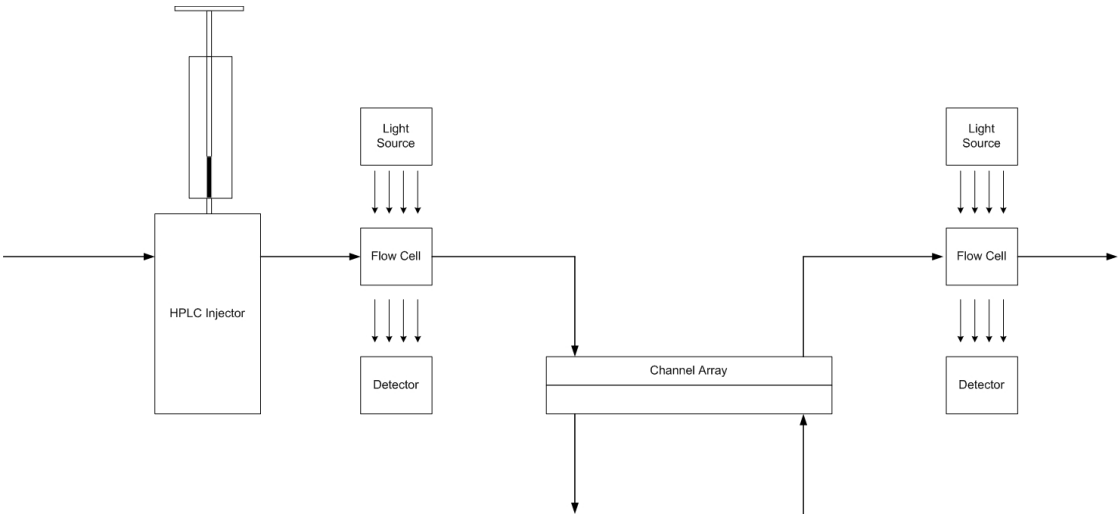


Figure 6.1: Pulse Test Apparatus

As can be seen from the input pulse shown previously, the Valco injector was very effective at generating a narrow distribution input pulse.

The detectors used were single wavelength spectrometers manufactured by [Corwin]. The low current signal output from the detectors were amplified by a custom amplification system [Flying Sparks Electronics]. This output was digitized at a sampling rate of 1kHz by a National Instruments DAQ-mx and recorded by NI-DAQmix. The choice of flow conditions and tracer was tailored to be as close as possible to the conditions where the experimental data was collected for

this device.

There are several requirements for a particular tracer to be effective. The tracer itself, a dye in this case, needs to be relatively non-interacting with the fluid. Any significant change in density or viscosity will lead to inaccurate results. It is also necessary that the effective diffusivity of the tracer in the membrane be as low as possible, to prevent tracer loss through diffusion. The tracer also must not adsorb onto the microchannel surface in way significant enough to change the apparent residence time. Finally, the tracer needs to be easily detectable at a sampling frequency that is much faster than the rise time of the pulse shapes. Blue dextran was chosen as a dye for these reasons. Since it has an extremely high molecular weight, it's effective diffusivity in the membrane is small. Blue dextran is very water soluble and has an intense color whose absorbance peak is close to the emitted wavelength of the detectors.

# Chapter 7 – Data

## 7.1 Finite Volume Simulation Data

An assumption inherent in the methods presented here is that the finite volume model accurately simulates the functioning of a single microchannel. All effects not taken into account by the model need to be trivial, otherwise error that is due to model inaccuracy will be attributed to flow maldistribution. The best means of validating this model is to compare the experimental results from a single microchannel to the model results. Unfortunately the flow rates from a single microchannel are so small that it would be difficult to accurately measure its performance. The only convenient way to test a microchannel's performance is to test a device with a small enough number channels that the distribution of channel velocities is so close to the ideal case that the flow distribution error is negligible. The data presented here was collected from a device with 26 channels which was directly machined and has an engineered header system to minimize flow maldistribution.

The simulation calculated the fluid dynamics and transport of scalar through the device for a single microchanel. The velocity field for a rectangular microchannel can be seen in Figure 7.1.

The flow in the x-direction is presented in Figure 7.2. The channel with positive

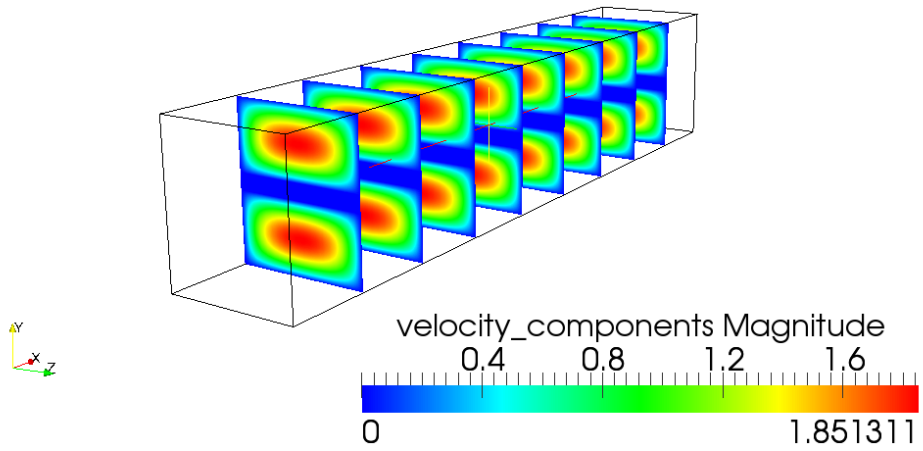


Figure 7.1: Slice plot of velocity magnitude for normalized velocity

flow is the blood channel, i.e. $C_o \neq 0$, while the negative flow channel has an inlet concentration of zero.

The y-direction component of flow determines the convective flux through the membrane. The normalized y-velocity can be seen in Figure 7.3.

A slice plot of the normalized z-direction flow is shown in Figure 7.4.

The velocity in the membrane is proportional to the trans membrane pressure drop. The velocity profile on the membrane centerline along the length of the microchannel is shown if Figure 7.5.

The transport of scalar within the device was calculated using the convection diffusion equation at the infinite dilution limit. The scalar field was evaluated using the calculated velocity field.

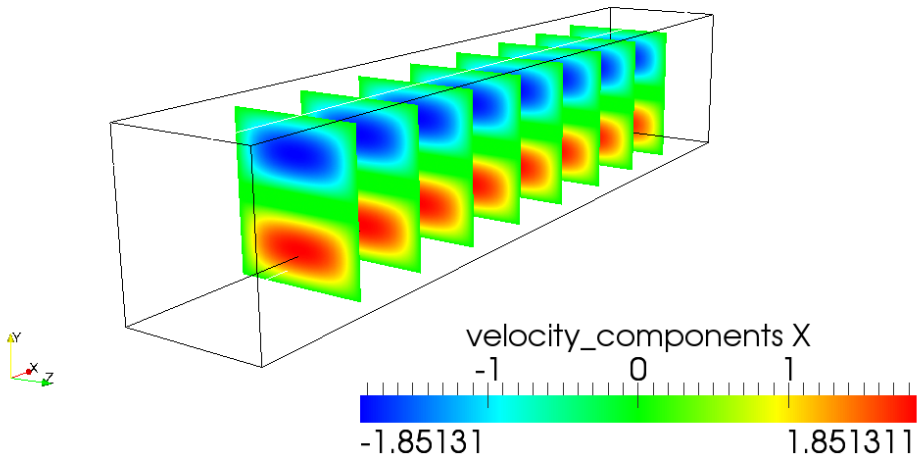


Figure 7.2: Slice plot of normalized x-velocity

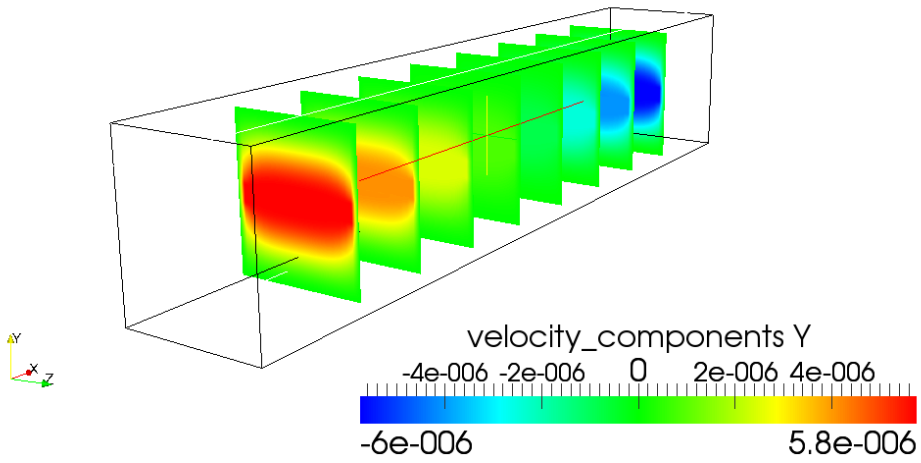


Figure 7.3: Slice plot of y-direction velocity

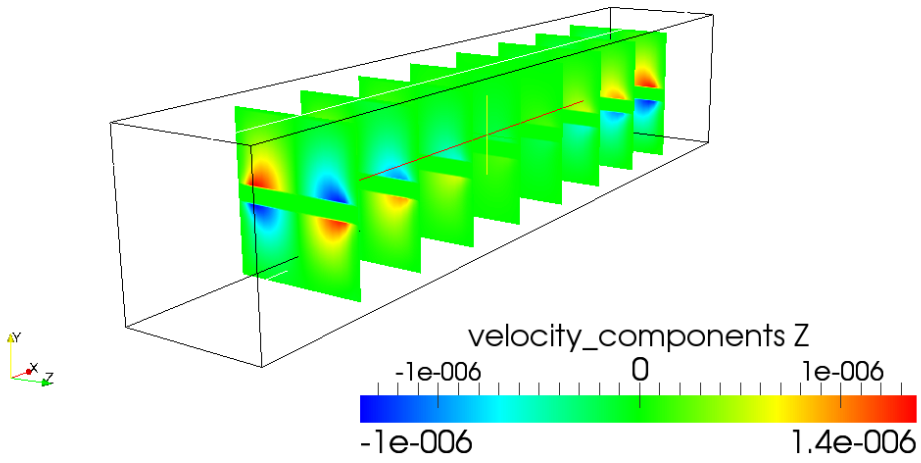


Figure 7.4: Slice plot of z-velocity

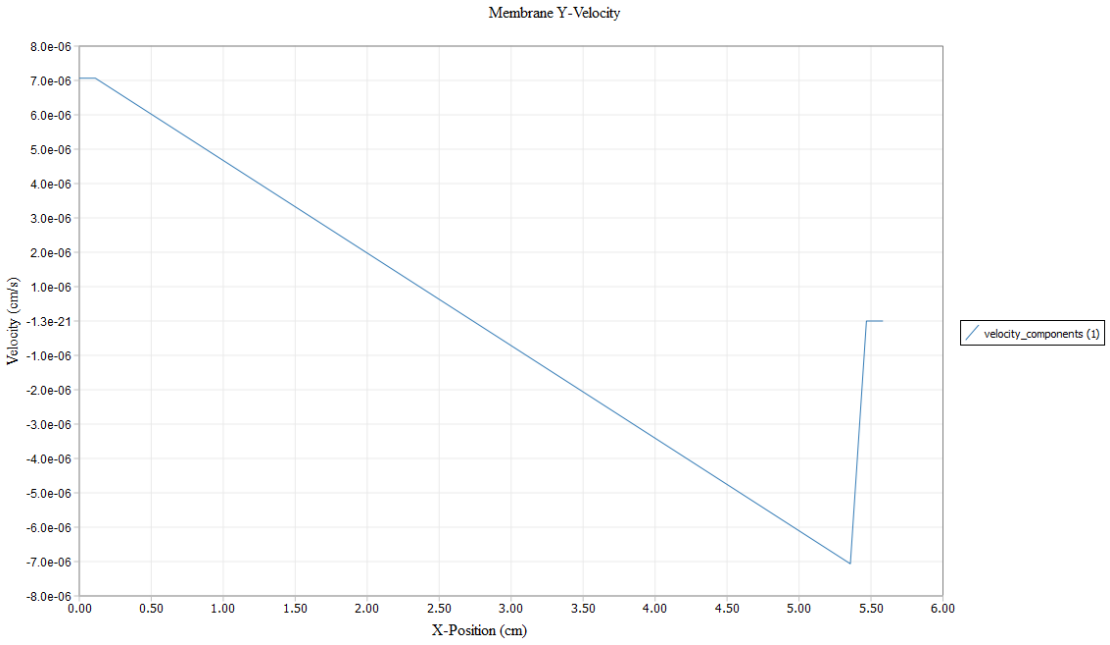


Figure 7.5: Y-Velocity in membrane along length of channel

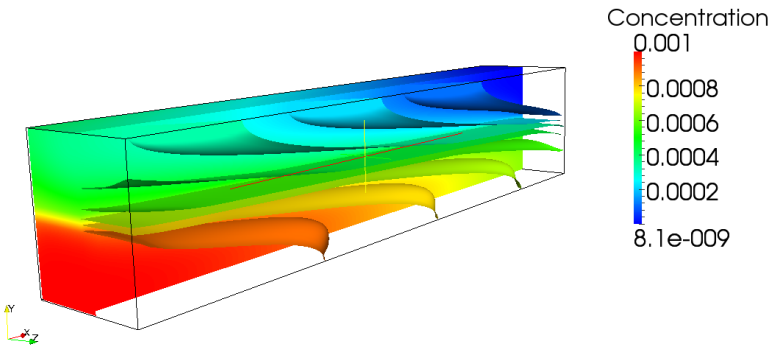


Figure 7.6: Concentration profile of the microchannal pair. Iso-surface and color by concentration.

A plot of the pressure profile in the device is presented in Figure 7.7.

The fractional removal for the device was calculated based on the convective fluxes out of the device relative to the inlet flux. The data shown below uses urea diffusion coefficients at 30 degrees Celsius, corrected from measured values at 25C using the Stokes-Einstein equation. The effective diffusivity in the membrane was calculated from published membrane resistances for the AN69 membrane. The simulation results compared to experimental data are shown in Figure 7.8.

As can be seen from the figure, there is extraordinarily good agreement between the simulation and experimental data. This lends some credence to the concept that the simulation results are a good representation of the actual device. Once this relation was established, an entire surface of fractional removals were calculated for the operational range of the microchannels. An example surface can be seen in Figure 7.9.

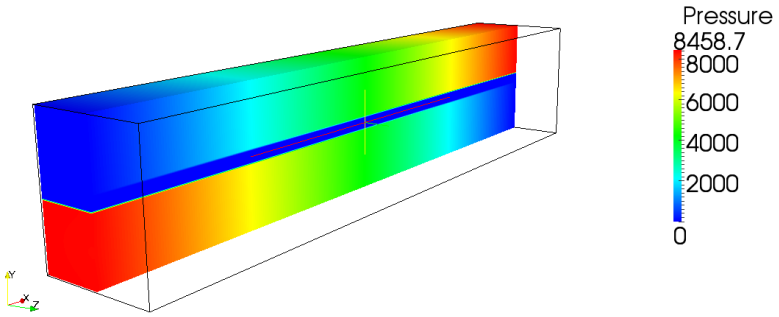


Figure 7.7: Pressure profile for 1 $\frac{cm}{s}$ and a channel length of 5.58 cm

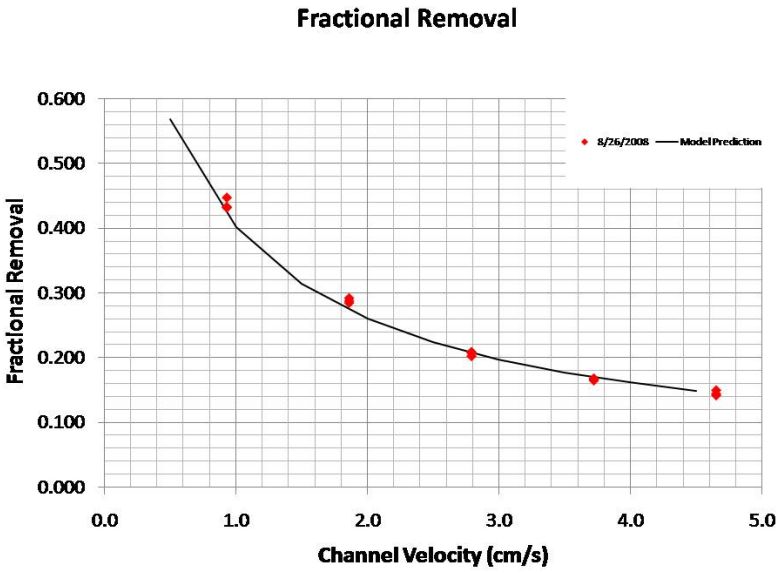


Figure 7.8: Model Results with Experimental Data

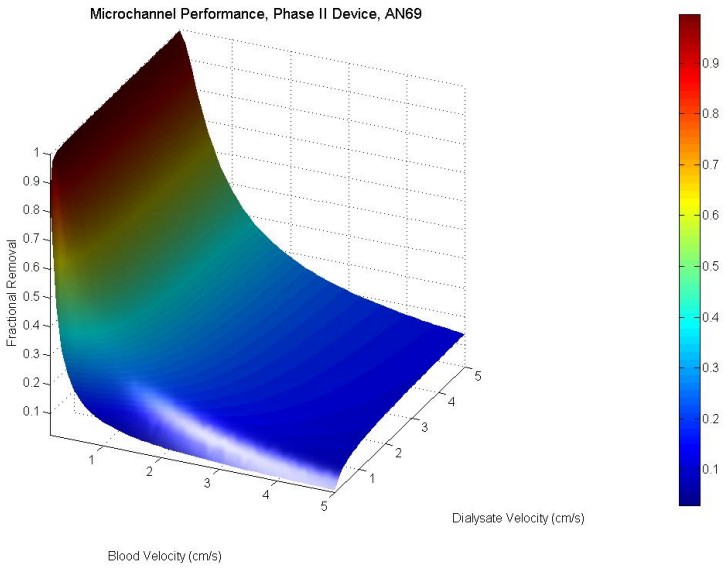


Figure 7.9: Fractional removal surface for a 5.58cm channel

This surface represents the predicted fractional removal at a given operating condition. The true performance surface of the device, however, must take into account the total amount of material removed from the channel. The surface corresponding to this condition is shown in Figure 7.10.

This surface allows for the calculation of the performance of a device that is made up of a plurality of microchannels at unique operating conditions within the operating range.

## 7.2 Velocity Distribution Data

One of the tools developed here is an algorithm that uses pulse test data to be able develop an estimate of the population of microchannel velocities. To be able to

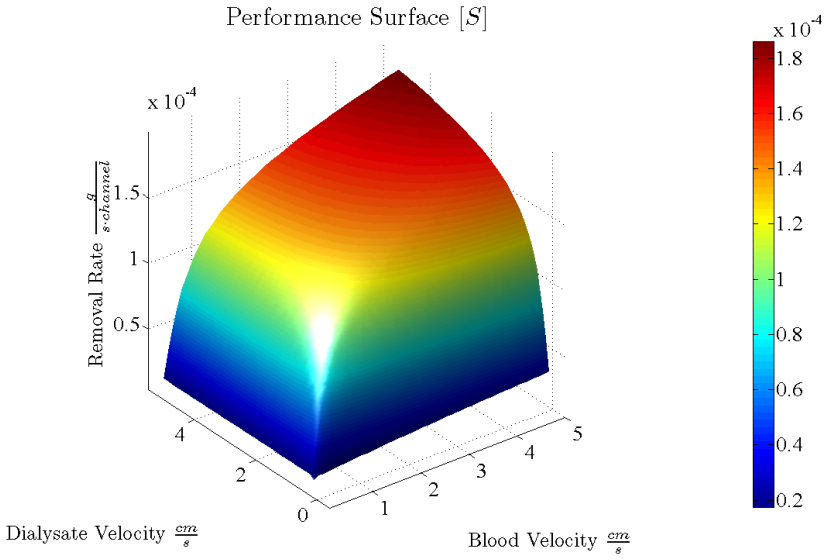


Figure 7.10: Performance surface $[S]$ for 5.58 cm channel. Note: z-axis units $\frac{g}{s \cdot channel}$

accomplish this it is necessary to have an estimate of the system response function. The output from an impulse response test would be equal to the system response test if the input pulse was a $\delta$ function. For the non-ideal case the output represents the convolution of the input pulse with the system response function. Example pulse response data can be seen in Figure 7.11.

Jannson's point iterative method is then used to attempt to generate an estimate of the system response function. The system response function for a 0.6 $\frac{ml}{min}$ pulse is shown in Figure 7.12.

Since there is an inherent amount of error present in the experimental data the residual for the solution process would stagnate before a 'vanishing' residual could be reached. In order to test for convergence the observed function was

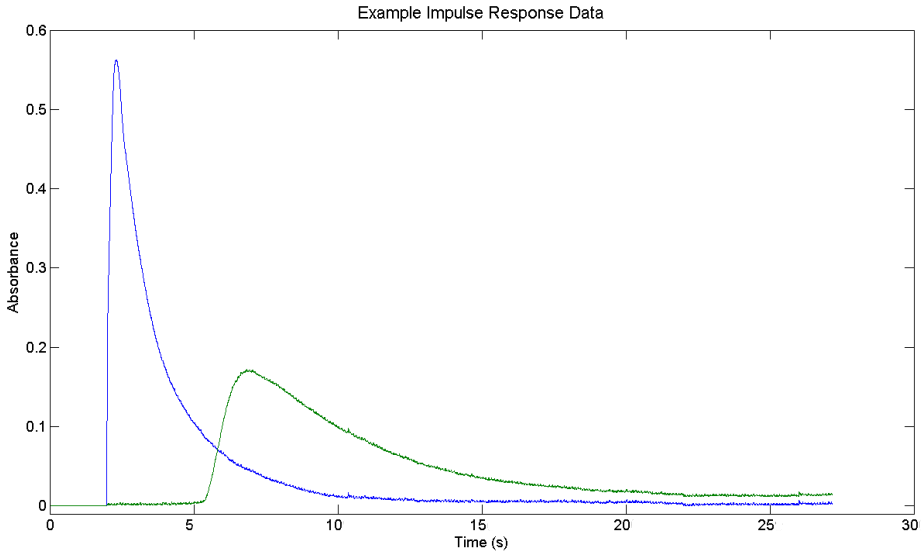


Figure 7.11: Impulse response experimental data

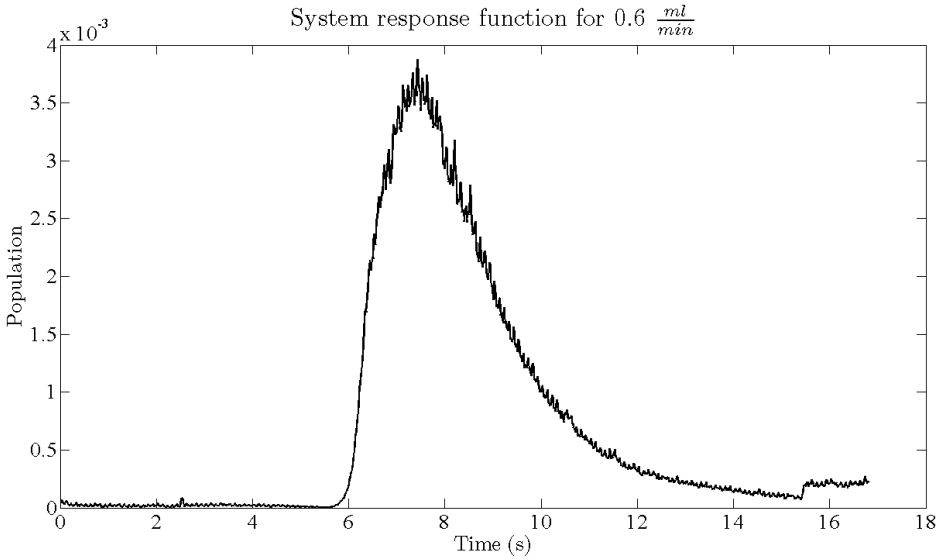


Figure 7.12: System response function for 0.6 $\frac{ml}{min}$

reconstructed using the input pulse and the system response function, and this result was then compared to recorded output pulse. The reconstructed image using the previous response function is shown in Figure 7.14.

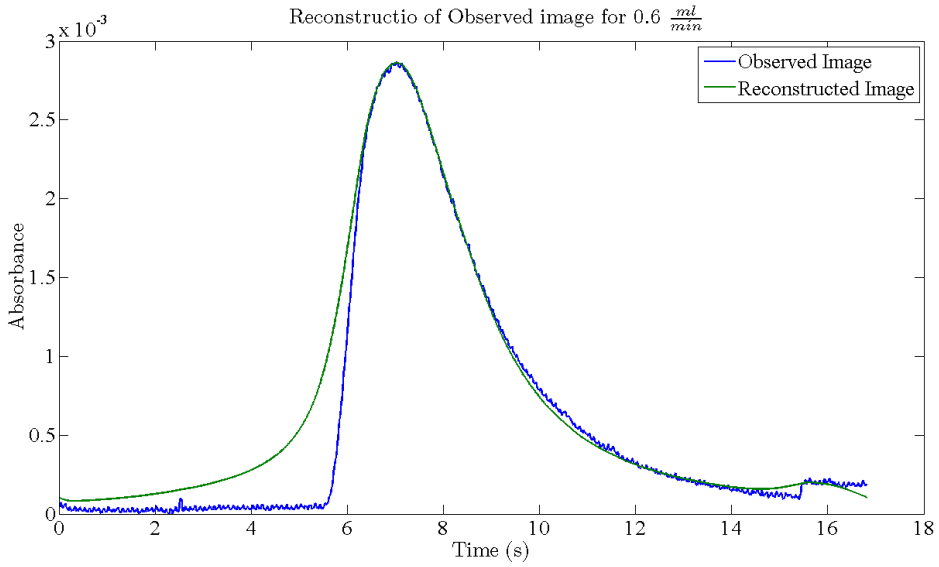


Figure 7.13: Image reconstructed from system response function compared to Observed image

There is obvious broadening in the reconstructed image, but overall the reconstruction is a good representation of the observed function. Once an accurate representation of the system response function is know; it can be converted to a velocity distribution. A representative distribution for 1 $\frac{ml}{min}$ can be seen in Figure 7.15. The ideal velocity for the system at this flowrate is about 3 seconds. This is easily within the range of calculated values.

The velocity distribution for the set of impulse response tests conducted can be found in Appendix C. The velocity distribution functions are generally of Gaussian

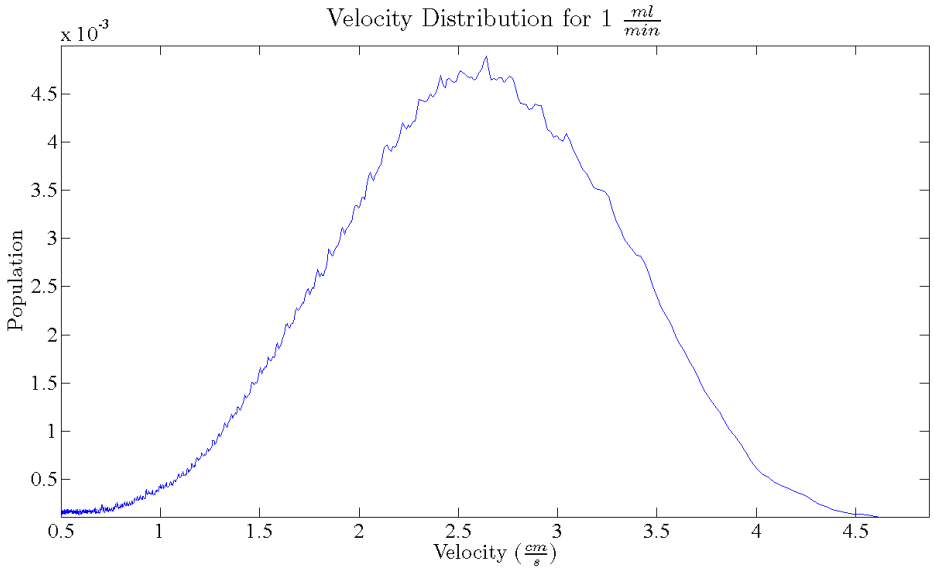


Figure 7.14: Velocity distribution for 1 $\frac{ml}{min}$

form, with variance that is necessarily velocity dependent.

## 7.3 Stochastic Model Data

The stochastic model uses a known distribution of microchannel velocities to generate sets of internal device states to find the most probable performance given that particular distribution. A parametric study was conducted, with the index of dispersion being the parameterized variable, to be able to identify the impact of index of dispersion on the fractional removal of the device. This parametric study is shown in Figure 7.15.

The stochastic model predicts a slight decrease in fractional removal overall. This tendency increases as the channel velocity is decreased and the curvature of

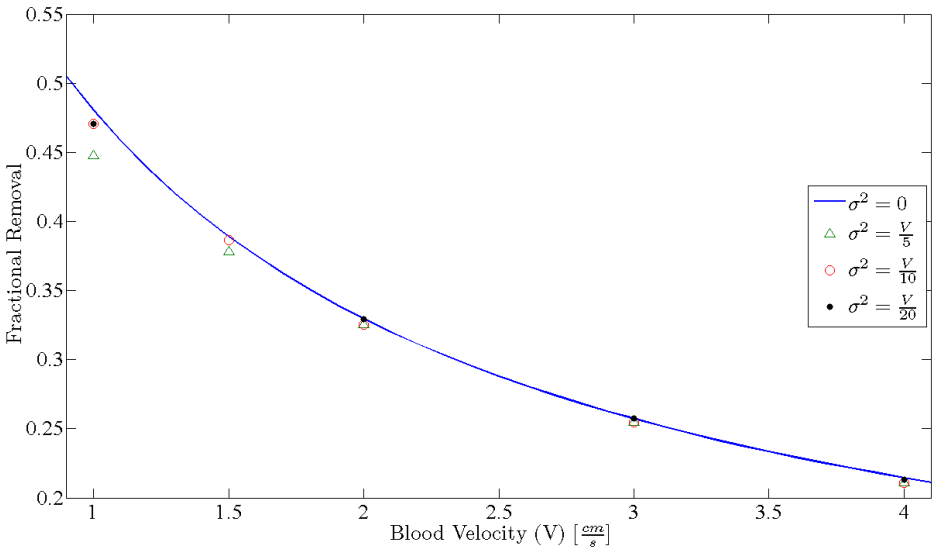


Figure 7.15: Comparison between stochastic removal data and finite volume simulation

the performance surface increases.

## 7.4 Analytical Solution

The analytic approach for determining the deviation of the real performance from the ideal yielded an that is linearly dependent on the variance for a constant curvature system. The Hessian of the performance surface, which describes the surfaces curvature, is not constant over the operating range. The Hessian is negative definite as low velocities, but the second partial derivative test fails far into the operating range. In actuality, both the jacobian and hessian approach zero as the velocities reach a critical magnitude and this influences the solution. A parametric

study in dispersion number was conducted. The fractional removal comparison for the ideal and non-ideal cases can be found in Figure 7.16.

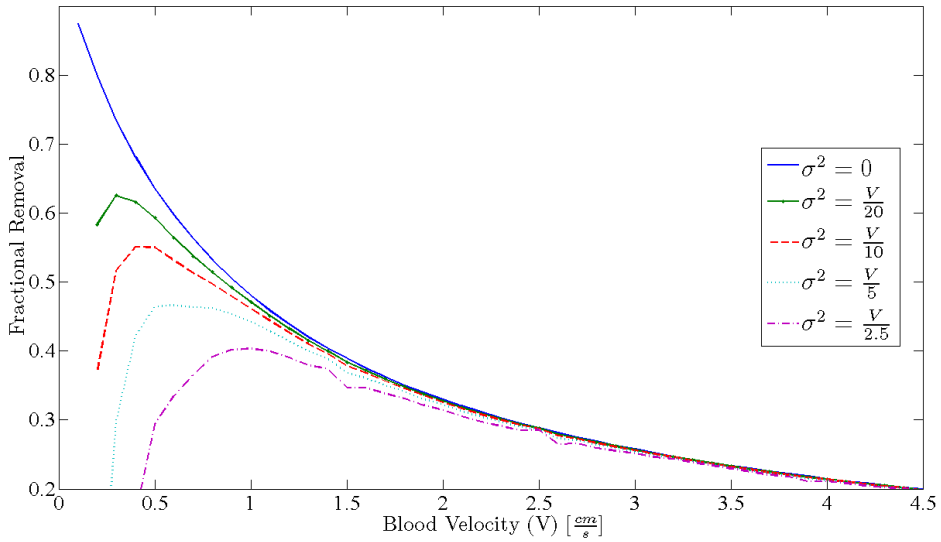


Figure 7.16: Comparison between finite volume and non-deal flow calculateion

It is apparent from the Figure that the deviation can be quite large as the velocity is decreased. The operating range of the device is determined by the minimum safe blood velocity, which is about 1 $\frac{cm}{s}$. So if the plot is rescaled to show the allowable operating range of the device then the true susceptibility of performance to flow distribution will be apparent.

If the data is inspected within the operating range of the device, it is apparent that the fractional removal is fairly insensitive to flow maldistribution. One of the initial conjectures of this work was that the device that was being used as a model was close enough to the ideal case that the simulation results could be directly compared with the experimental data. This appears to be a valid assumption not

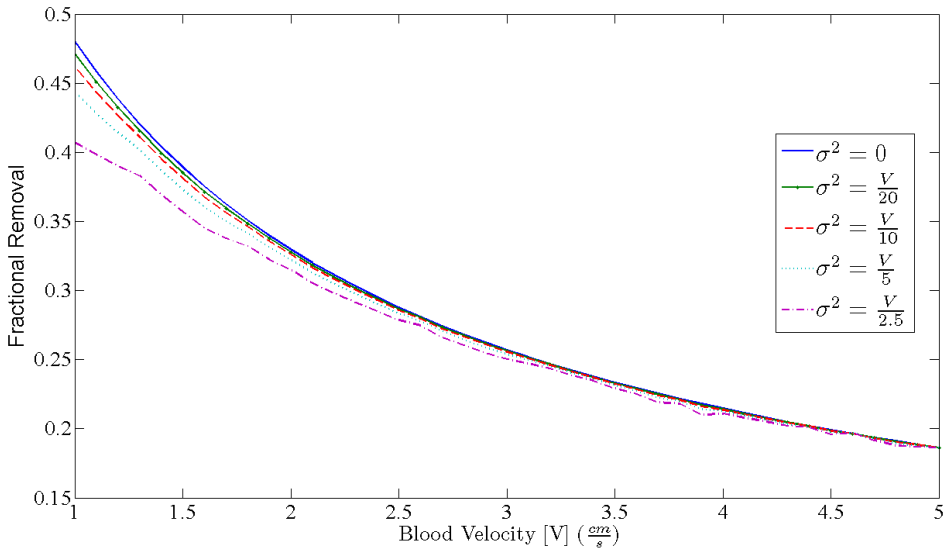


Figure 7.17: Comparison of ideal and non-ideal simulation results within the operating range of the test device

because the flow distribution is close to ideal, but because the performance surface has too little curvature to allow large perturbations in fractional removal.

## 7.5 Comparison of Stochastic and Continuum Methods

Parametric studies were conduction with both the analytic and stochastic methods to determine the impact of flow maldistribution on device performance. Since the studies were done with identical indexes of dispersion and zero and uncorrelated data, they should yield similar reductions in fractional removal with respect to velocity and index of dispersion. A comparison of the two methods for an index of dispersion of 0.2 with the finite volume simulation is shown in Figure 7.18.

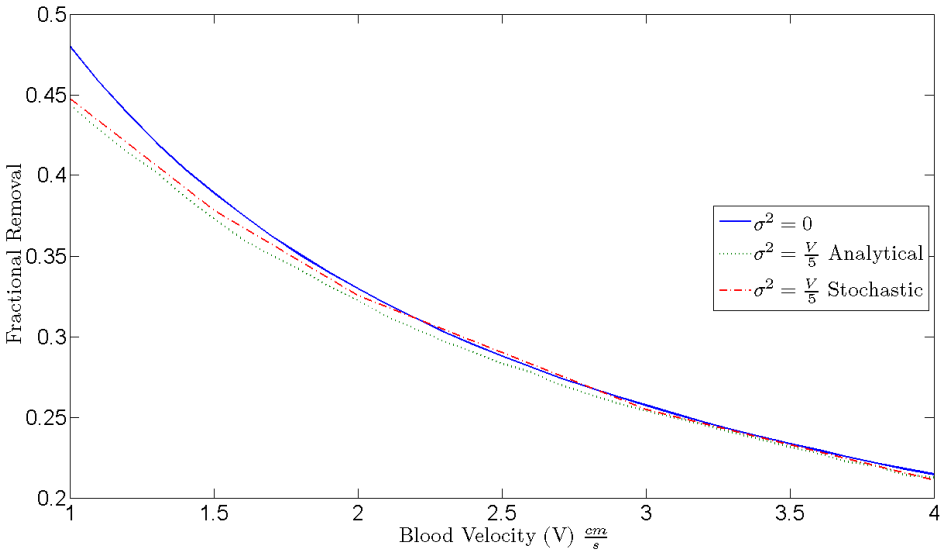


Figure 7.18: Comparison of stochastic and analytic results at an index of dispersion of 0.2 to finite volume simulation

The two methods agree quite well in the operating range, limiting to nearly identical values for 1 $\frac{cm}{s}$. A comparison of the two methods at a index of dispersion of 0.1 can be found in Figure 7.19.

Again, the two methods are in agreement on the reduction in fractional removal. The values are almost identical for the low end of the operating range, which is the range susceptible to flow maldistribution.

## 7.6 Comparison Between Simulations and Experimental Data

The models presented here are in general agreement on the reduction of fractional removal at a given distribution of flowrates. In Figure 7.20 a comparison between

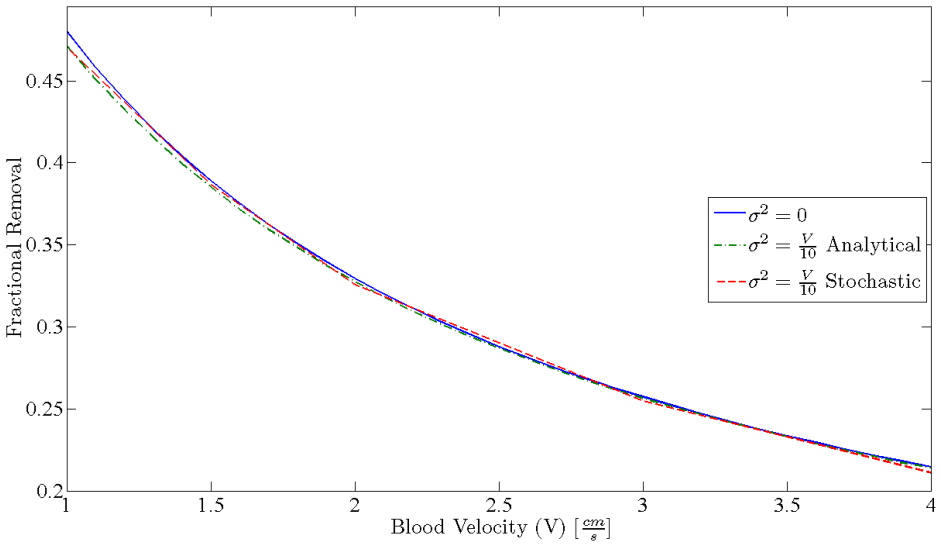


Figure 7.19: Comparison of stochastic and analytic models at a index of dispersion of 0.1

the simulation results and experimental data is shown.

Even with the decrease in fractional removal predicted by both methods the simulation data is still slightly higher than the experimental data. The velocities for which velocity populations could be measured are in the flow regime where the decrease predicted by the models is much below experimental error.

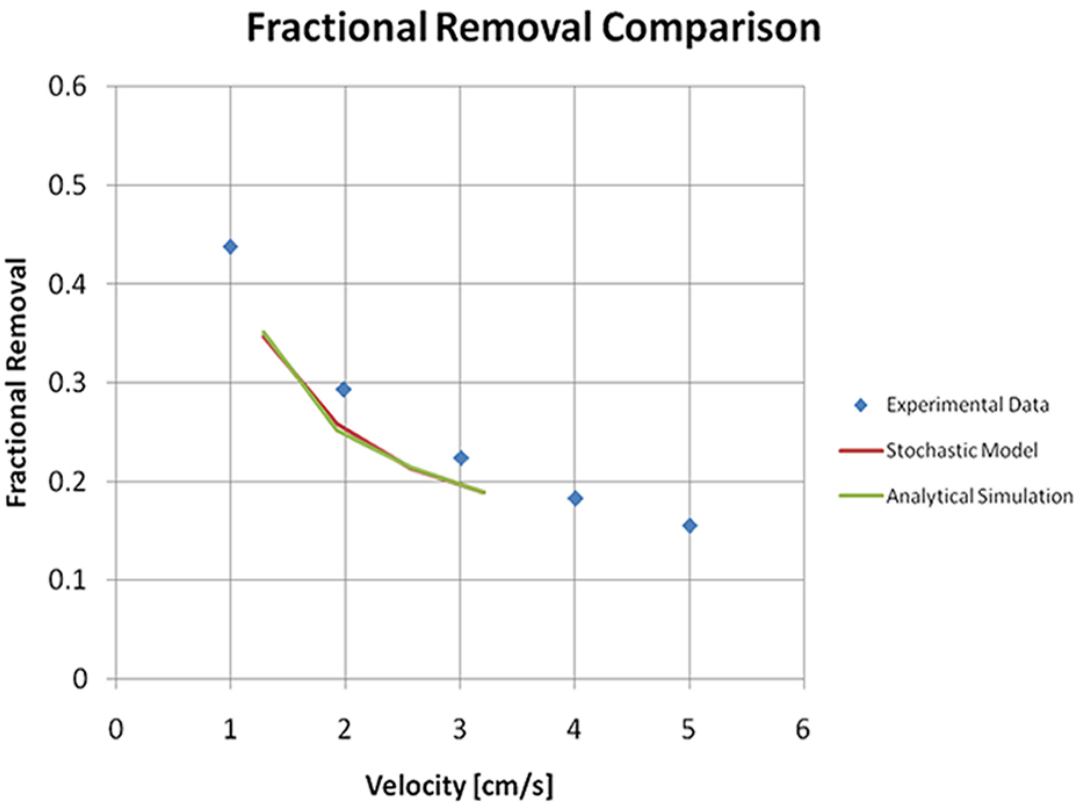


Figure 7.20: Comparison between experimental data and model results

# Chapter 8 – Conclusions

This study attempted to find a means of calculating the impact of flow maldistribution on the performance of a microfluidic array. It is necessary to have both an approximation of the performance characteristics of the array as well as the velocity distribution of the channels in the array. A finite volume simulation was developed to be able to predictively generate the performance surface for the device. The simulation results compared favorably to experimental data. To be able to generate the vast amount of data needed for the stochastic simulation in a reasonable amount of time it was necessary to write the simulation in FORTRAN using Intel's Math Kernel Libraries optimized linear solvers.

A deconolution method was implemented attempted in order to recover the system response function and then derive the velocity distribution. The deconvolution algorithm was successful in converging to a reasonable approximation to the system response function. The velocity distribution was then calculated using the computed system response function. This distribution was then used to generate fractional removal data using both the stochastic and analytic models. Parametric studies using index of dispersion, $I_d$, as the parameterized variable to be able to generalize the ipact of velocity distribution on performance.

The stochastic simulation predicted an overall decrease in fractional removal as the variance increased. The decrease is highly correlated with the Hessian

of the performance curve in the vicinity of the expected value of the velocity distribution. Regions of high second order curvature were more susceptible to flow maldistribution than are regions of low or zero curvature. The simulation results were in good agreement with experimental data, but for this system extremely channel velocities would be necessary to be able to benchmark the method.

If the distribution of microchannel velocities is simplified to the normal bivariate case, then an analytic approach to characterizing the performance impact of flow maldistribution can be taken. By using a second order Taylor expansion to approximate the performance surface in the vicinity of the operating point, it is possible to get an analytic representation of the deviation surface. The integral of this surface gives the absolute deviation of the system with respect to the ideal. This representation led to the generation of two useful relations. The first is that the ability to determine the sign of $\mathfrak{D}$ by the eigenvalues of the Hessian of Taylor series, and the second is an equation relating $\mathfrak{D}$ to the Hessian and the variance of the velocity distribution. To compare this model to experimental data, the variances for the experimentally determined distribution were evaluated using the Hessian from the finite volume simulation. This data agreed perfectly with the stochastic model, and slightly overpredicted the actual fractional removal.

$$\mathfrak{D} = \frac{1}{2}\left[\sigma_u^2 \frac{\partial^2 f(u_s, v_s)}{\partial u^2} + 2\sigma_u \sigma_v \frac{\partial^2 f(u_s, v_s)}{\partial u \partial v} + \sigma_v^2 \frac{\partial^2 f(u_s, v_s)}{\partial v^2}\right] \tag{8.1}$$

$$\begin{array}{lll} det(H) > 0 & \frac{\partial^2 f(u_s,v_s)}{\partial u^2} > 0 & \mathfrak{D} > 0 \\ det(H) > 0 & \frac{\partial^2 f(u_s,v_s)}{\partial u^2} < 0 & \mathfrak{D} < 0 \\ det(H) < 0 & & \text{saddle point} \\ det(H) = 0 & & \text{indeterminant} \end{array} \tag{8.2}$$

# APPENDICES

# Appendix A – Nomenclature

| Symbol | Units | Description |
|---|---|---|
| $A$ | | General n by n coefficient matrix |
| $A_c$ | $cm^2$ | Cross sectional area |
| $C$ | $\frac{g}{cm^3}$ | Concentration |
| $D$ | $\frac{cm^2}{s}$ | Diffusivity of solute in solvent |
| $D_{eff}$ | $\frac{cm^2}{s}$ | Effective diffusivity of solute in membrane |
| $f(u,v)$ | $\frac{g}{s \cdot channel}$ | Performance surface of a microchannel at point (u,v) |
| $F_r$ | $dimensionless$ | Fractional removal of solute from the device |
| $H_p$ | $\frac{Q}{\Delta P}$ | Hydraulic Permeability of the membrane |
| $H$ | | Hessian matrix |
| $I_d$ | $dimensionless$ | Index of dispersion |
| $i(t)$ | $absorbance$ | Input pulse |
| $n$ | $dimensionless$ | Channel Index |
| $o(t)$ | $absorbance$ | Observed pulse response output image |
| $P(u,v)$ | $dimensionless$ | Distribution of microchannel velocities |
| $P$ | $Pa$ | Pressure |
| $P'$ | $Pa$ | Pressure correction term |

(A.1)

| Symbol | Units | Description |
|---|---|---|
| $Q$ | $\frac{ml}{min}$ | Flow rate |
| $S(u,v)$ | $\frac{g}{s \cdot channel}$ | The performance surface of the device |
| $s(t)$ | $absorbance$ | System response function |
| $t$ | $s$ | Time |
| $\overline{u}$ | $\frac{cm}{s}$ | mean velocity |
| $u$ | $\frac{cm}{s}$ | x-velocity component |
| $u_s$ | $\frac{cm}{s}$ | Operating condition set point |
| $v$ | $\frac{cm}{s}$ | y-velocity component |
| $v_s$ | $\frac{cm}{s}$ | Operating condition set point |
| $w$ | $\frac{cm}{s}$ | z-velocity component |
| $\Theta$ | | Error whose integral is zero |
| $\rho$ | | correlation coefficient |
| $\sigma_i$ | | Standard deviation in the i-th direction |
| $\sigma_i^2$ | | Variance in the $i^{th}$ direction |
| $\mathbf{\Sigma}$ | | Covariance matrix |
| $\Sigma$ | | sum |
| $\tau$ | $s$ | dummy variable for convolution integral |
| $\mu$ | | Expected value |
| $\mathfrak{D}$ | $\frac{g}{s}$ | Devation function for the flow maldistributed case |
| $\mathfrak{S}$ | $\frac{g}{s}$ | Overall Device Performance |

(A.2)

# Appendix B – Derivation of Deviation Function

To start the derivation it is necessary to be able to algebraically represent each surface. If the device under consideration can be assumed to have a large number of channels and no systemic manufacturing errors, then a bivariate normal distribution should give a reasonable representation of the surface. For the performance surface the case is not as straightforward since it will likely be either generated numerically from a simulation or experimentally determined. In either case it is unlikely that a global performance surface will be known, so it must be approximated using what is known about the local performance characteristics. In this study a multivariate Taylor series expansion will be used to approximate the surface in the vicinity of the operating point.

Start with the bivariate normal distribution [8].

$$P(u,v) = \frac{1}{2\pi\sigma_u\sigma_v} e^{\frac{1}{2\sqrt{1-\rho^2}}(\frac{(u-u_s)^2}{\sigma_v^2}+\frac{(v-v_s)^2}{\sigma_v^2}-\frac{2\rho(u-u_s)(v-v_s)}{\sigma_u sigma_v})} \tag{B.1}$$

To simplify the following variable change can be used [10].

$$\begin{aligned} x &= u - u_s \\ y &= v - v_s \\ A &= \frac{1}{2\pi\sigma_u\sigma_v} \end{aligned} \tag{B.2}$$

The distribution function then simplifies to:

$$P(x,y) = Ae^{\frac{1}{2\sqrt{1-\rho^2}}(\frac{x^2}{\sigma_x^2}+\frac{y^2}{\sigma_y^2}-\frac{2\rho xy}{\sigma_x\sigma_y})} \tag{B.3}$$

It should be noted that the variable substitution only moves the expected value of the distribution to $(0,0)$, but does not alter the distribution itself. Therefore the variances should be equivalent.

$$\begin{aligned} \sigma_x &= \sigma_u \\ \sigma_y &= \sigma_v \end{aligned} \tag{B.4}$$

This allows the description of the distribution with two degrees of freedom. Now to approximate the performance space a generalized bivariate Taylor expansion is [22]:

$$\begin{aligned} f(u,v) =& f(u_s,v_s) + (u-u_s)\frac{\partial f(u_s,v_s)}{\partial u} + (v-v_s)\frac{\partial f(u_s,v_s)}{\partial v} + \\ & \frac{1}{2}[(u-u_s)^2\frac{\partial^2 f(u_s,v_s)}{\partial u^2} + 2(u-u_s)(v-v_s)\frac{\partial^2 f(u_s,v_s)}{\partial u \partial v} \\ & (v-v_s)^2\frac{\partial^2 f(u_s,v_s)}{\partial v^2}] \end{aligned} \tag{B.5}$$

Now this expression can undergo the simplifying variable substitution [10].

$$f(x,y) = f(u_s,v_s) + x\frac{\partial f(u_s,v_s)}{\partial u} + y\frac{\partial f(u_s,v_s)}{\partial v} + \frac{1}{2}[x^2\frac{\partial^2 f(u_s,v_s)}{\partial u^2} + 2xy\frac{\partial^2 f(u_s,v_s)}{\partial x \partial v} + y^2\frac{\partial^2 f(u_s,v_s)}{\partial v^2}] \tag{B.6}$$

So then the performance distribution will then be the product of the microchannel flow distribution and the performance surface.

$$\begin{aligned} P(x,y)f(x,y) = & Af(u_s,v_s)e^{-\frac{1}{2\sqrt{1-\rho^2}}(\frac{x^2}{\sigma_x}+\frac{y^2}{\sigma_y}-\frac{2\rho xy}{\sigma_x\sigma_y})} + \\ & Ax\frac{\partial f(u_s,v_s)}{\partial u}e^{-\frac{1}{2\sqrt{1-\rho^2}}(\frac{x^2}{\sigma_x}+\frac{y^2}{\sigma_y}-\frac{2\rho xy}{\sigma_x\sigma_y})} + \\ & Ay\frac{\partial f(u_s,v_s)}{\partial v}e^{-\frac{1}{2\sqrt{1-\rho^2}}(\frac{x^2}{\sigma_x}+\frac{y^2}{\sigma_y}-\frac{2\rho xy}{\sigma_x\sigma_y})} + \\ & \frac{A}{2}[x^2\frac{\partial^2 f(u_s,v_s)}{\partial u^2}e^{-\frac{1}{2\sqrt{1-\rho^2}}(\frac{x^2}{\sigma_x}+\frac{y^2}{\sigma_y}-\frac{2\rho xy}{\sigma_x\sigma_y})} + \\ & xy\frac{\partial^2 f(u_s,v_s)}{\partial u \partial v}e^{-\frac{1}{2\sqrt{1-\rho^2}}(\frac{x^2}{\sigma_x}+\frac{y^2}{\sigma_y}-\frac{2\rho xy}{\sigma_x\sigma_y})} + \\ & y^2\frac{\partial^2 f(u_s,v_s)}{\partial v^2}e^{-\frac{1}{2\sqrt{1-\rho^2}}(\frac{x^2}{\sigma_x}+\frac{y^2}{\sigma_y}-\frac{2\rho xy}{\sigma_x\sigma_y})}] \end{aligned} \tag{B.7}$$

Now Equation B.7 needs to be integrated over all space. This will allow the evaluation of integrals involving $e^{-x^2}$ without the use of the error function. The following identities are used for the evaluation of the integral [22].

$$\int_{-\infty}^{\infty} e^{\frac{x^2}{\sigma_x^2}} = \sqrt{\pi}\sigma_x \tag{B.8}$$

$$\int_{-\infty}^{\infty} x e^{\frac{x^2}{\sigma_x^2}} = 0 \tag{B.9}$$

$$\int_{-\infty}^{\infty} x^2 e^{\frac{x^2}{\sigma_x^2}} = \frac{\sqrt{\pi}\sigma_x^3}{2} \tag{B.10}$$

$$\tag{B.11}$$

The integral of each term in Equation B.7 then are:

$$\iint_{-\infty}^{\infty} e^{-\frac{1}{2\sqrt{1-\rho^2}}(\frac{x^2}{\sigma_x^2}+\frac{y^2}{\sigma_y^2}-\frac{2\rho xy}{\sigma_x\sigma_y})} = 2\pi\sigma_x\sigma_y\sqrt{1-\rho^2} \tag{B.12}$$

$$\iint_{-\infty}^{\infty} x e^{-\frac{1}{2\sqrt{1-\rho^2}}(\frac{x^2}{\sigma_x^2}+\frac{y^2}{\sigma_y^2}-\frac{2\rho xy}{\sigma_x\sigma_y})} = 0 \tag{B.13}$$

$$\iint_{-\infty}^{\infty} y e^{-\frac{1}{2\sqrt{1-\rho^2}}(\frac{x^2}{\sigma_x^2}+\frac{y^2}{\sigma_y^2}-\frac{2\rho xy}{\sigma_x\sigma_y})} = 0 \tag{B.14}$$

$$\iint_{-\infty}^{\infty} xy e^{-\frac{1}{2\sqrt{1-\rho^2}}(\frac{x^2}{\sigma_x^2}+\frac{y^2}{\sigma_y^2}-\frac{2\rho xy}{\sigma_x\sigma_y})} = 2\pi\rho\sigma_x^2\sigma_y^2\sqrt{1-\rho^2} \tag{B.15}$$

$$\iint_{-\infty}^{\infty} x^2 e^{-\frac{1}{2\sqrt{1-\rho^2}}(\frac{x^2}{\sigma_x^2}+\frac{y^2}{\sigma_y^2}-\frac{2\rho xy}{\sigma_x\sigma_y})} = 2\pi\sigma_x^3\sigma_y\sqrt{1-\rho^2} \tag{B.16}$$

$$\iint_{-\infty}^{\infty} y^2 e^{-\frac{1}{2\sqrt{1-\rho^2}}(\frac{x^2}{\sigma_x^2}+\frac{y^2}{\sigma_y^2}-\frac{2\rho xy}{\sigma_x\sigma_y})} = 2\pi\sigma_x\sigma_y^3\sqrt{1-\rho^2} \tag{B.17}$$

Subsituting these values into the original integral expression. Now call the surface distribution $S(x, y)$.

$$S(x, y) = P(x, y)f(u, v) \tag{B.18}$$

$$\iint_{-\infty}^{\infty} S(x,y) = A2\pi\sigma_x\sigma_y\sqrt{1-\rho^2}f(u_s,v_s) + \frac{A}{2}[\pi\sigma_x^3\sigma_y\sqrt{1-\rho^2}\frac{\partial^2 f(u_s,v_s)}{\partial u^2} + 4\pi\rho\sigma_x^2\sigma_y^2\sqrt{1-\rho^2}\frac{\partial^2 f(u_s,v_s)}{\partial u\partial v} + 2\pi\sigma_x\sigma_y^3\sqrt{1-\rho^2}\frac{\partial^2 f(u_s,v_s)}{\partial v^2}] \tag{B.19}$$

And the integrated area is:

$$\iint_{-\infty}^{\infty} S(x,y)dxdy = \mathfrak{S} \tag{B.20}$$

Now return substitution variable $A$ to native variables.

$$\iint_{-\infty}^{\infty} S(x,y) = f(u_s,v_s) + \frac{1}{2}[\sigma_x^2\frac{\partial^2 f(u_s,v_s)}{\partial u^2} + 2\rho\sigma_x\sigma_y\frac{\partial^2 f(u_s,v_s)}{\partial u\partial v} + \sigma_y^2\frac{\partial^2 f(u_s,v_s)}{\partial v^2}] \tag{B.21}$$

In order to analyze this surface it is necessary to be able to compare it against a case where the flow distribution is perfect. Taking the limit of equation XXX as $\sigma_x^2$ and $\sigma_y^2$ goes to zero.

$$\lim_{\sigma_x\to 0}\left(\lim_{\sigma_y\to 0} f(u_s,v_s) + \frac{1}{2}[\sigma_x^2\frac{\partial^2 f(u_s,v_s)}{\partial u^2} + 2\rho\sigma_x\sigma_y\frac{\partial^2 f(u_s,v_s)}{\partial u\partial v} + \sigma_y^2\frac{\partial^2 f(u_s,v_s)}{\partial v^2}]\right) \tag{B.22}$$

Which obviously becomes:

$$f(u_s, v_s) \tag{B.23}$$

So the deviation between the ideal and nonideal case would then be:

$$\mathfrak{D} = \mathfrak{S} - \lim_{(\sigma_x, \sigma_y) \to 0} (\mathfrak{S}) \tag{B.24}$$

$$\mathfrak{D} = f(u_s, v_s) + \frac{1}{2}[\sigma_x^2 \frac{\partial^2 f(u_s, v_s)}{\partial u^2} + 2\sigma_x \sigma_y \frac{\partial^2 f(u_s, v_s)}{\partial u \partial v} \sigma_y^2 \frac{\partial^2 f(u_s, v_s)}{\partial v^2} - f(u_s, v_s) \tag{B.25}$$

$$\mathfrak{D} = \frac{1}{2}\left[\sigma_x^2 \frac{\partial^2 f(u_s, v_s)}{\partial u^2} + 2\sigma_x \sigma_y \frac{\partial^2 f(u_s, v_s)}{\partial u \partial v} + \sigma_y^2 \frac{\partial^2 f(u_s, v_s)}{\partial v^2}\right] \tag{B.26}$$

# Appendix C – Velocity Distribution Data

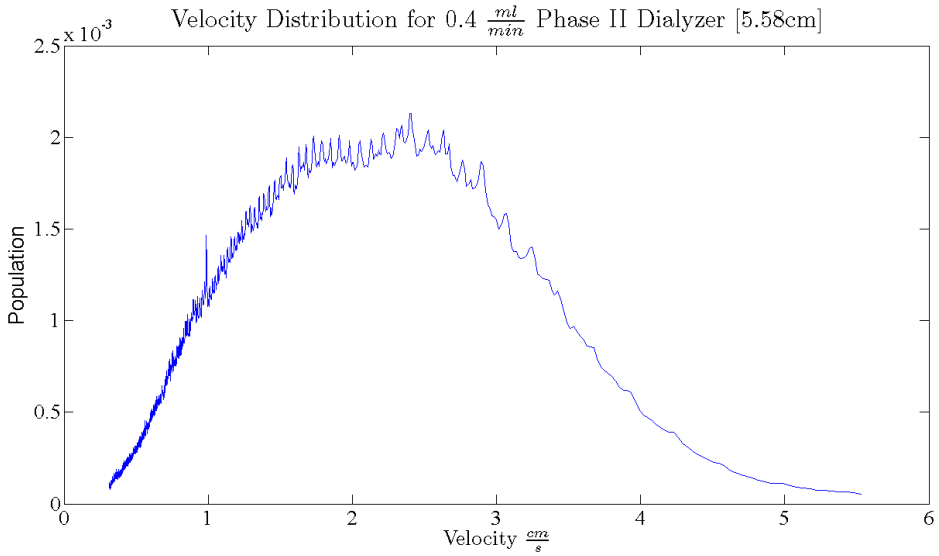


Figure C.1: Velocity Distribution for 0.4 $\frac{ml}{min}$ Phase II Dialyzer [5.58cm]

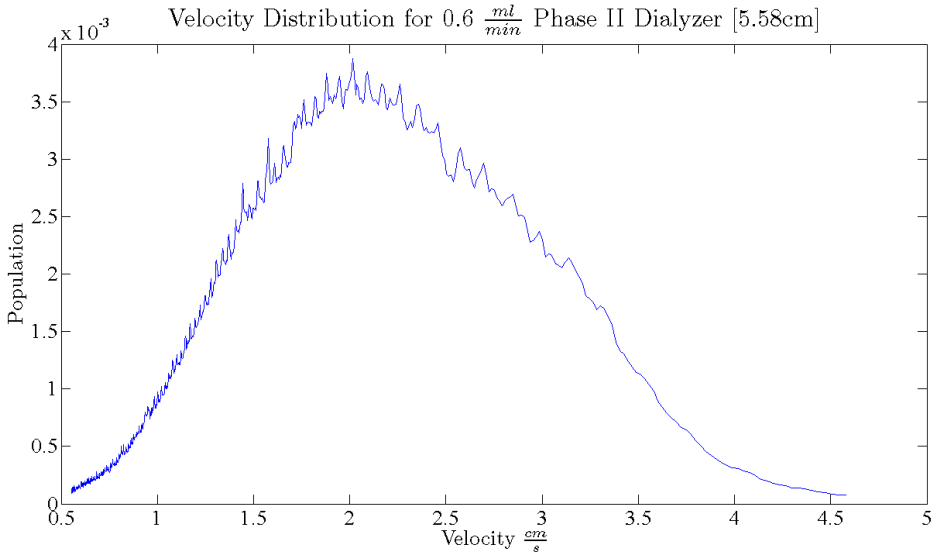


Figure C.2: Velocity Distribution for 0.6 $\frac{ml}{min}$ Phase II Dialyzer [5.58cm]

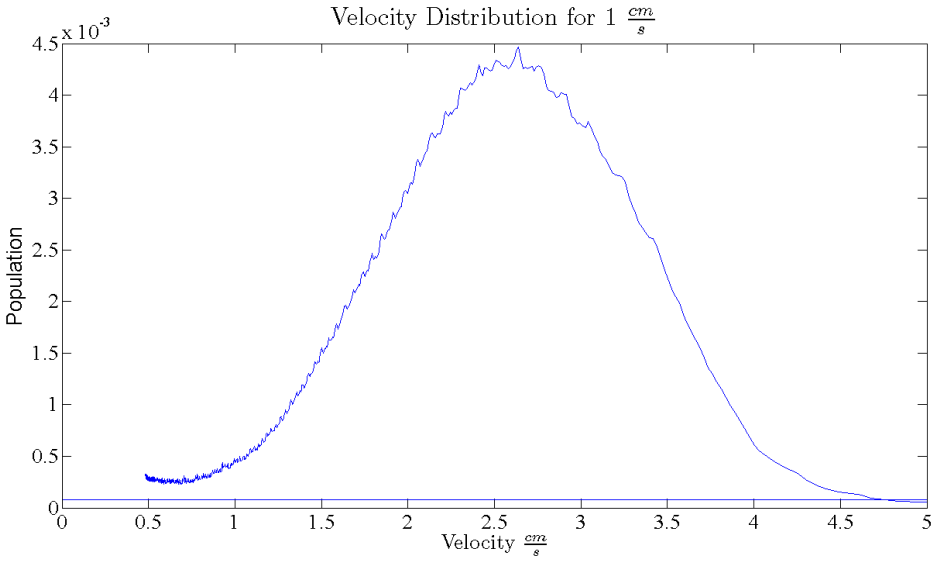


Figure C.3: Velocity Distribution for 1 $\frac{ml}{min}$ Phase II Dialyzer [5.58 cm]

# Bibliography

[1] Tom M. Apostol. *Mathematical Analysis*. Addison Wesley Longman, second edition, 1974.

[2] I.E. Barton. Comparison of simple and piso-type algorithms for transient flows. *International Journal for Numerical Methods In Fluids*, 26:459–483, 1998.

[3] Michele Benzi. Preconditioning techniques for large linear systems: A survey. *Journal of Computational Physics*, 182:418–477.

[4] Michael C. Collins and W. Fred Ramirez. Mass transport in polymeric membranes. *Journal of Physical Chemistry*, 83:2294–2301, 1979.

[5] E.L. Cussler. *Diffusion: Mass Transfer in Fluid Systems*. Cambridge University Press, second edition, 1997.

[6] Germund Dahlquist and Ake Bjorck. *Numerical Methods in Scientific Computing*. Society for Industrial and Applied Mathematics, 2008.

[7] J.H. Ferzinger and M. Peric. *Computational Methods for Fluid Dynamics*. Springer, third edition, 2002.

[8] G.G. Hamedani and M.N. Tata. On the determination of the bivariate normal distribution from distributions of linear combinations of the variables. *The American Mathematical Monthly*, 82:913–915, 1975.

[9] T Hayase, J.A.C. Humphrey, and R. Greif. A consistently formulated quick scheme for fast and stable convergence using finite-volume iterative calculation procedures. *Journal of Computational Physics*, 98:108–118, 1992.

[10] Eugene Jahnke and Fritz Emde. *Tables of Functions With Formulae and Curves (Funktionentafeln)*. Dover Publications, 1943.

[11] Peter Jansson. *Deconvolution With Applications in Spectroscopy*. Academic Press, Inc, 1984.

[12] Peter Jansson, Robert H. Hunt, and Earle K. Plyler. Resolution enhancement of spectra. *Journal of the Optical Society of America*, 60:595–599, 1970.

[13] Klavs F. Jensen. Microreaction engineering-is small better. *Chemical Engineering Science*, 56, 2001.

[14] Octave Levenspiel. *Chemical Reaction Engineering*. Wiley, third edition, 1998.

[15] Fausto Millanazzo, Cedric Zala, and Ian Barrodale. On the rate of growth of condition numbers for convolution matrices. *IEEE Transactions on Acoustics, Speech, and Signal Processing*, 35:471–475, 1987.

[16] Brian Paul and Richard B. Peterson. Microlamination for microtechnology-based engergy, chemical, and biological systems. *International Mechanical Engineering Congress and Exposition*, 39:45–52, 1999.

[17] Hirohiko Shima. Hessian manifolds of constant hessian sectional curvature. *Journal of the Mathematical Society of Japan*, 47, 1995.

[18] H.K Versteeg. *An introduction to Computational Fluid Dynamics The Finite Volume Method*. Prentice Hall, 2007.

[19] Alana Warner-Tuhy. Mass transfer of urea, creatinine, and vitamin b12 in a microchannel based membrane separation unit. *Oregon State University*, 2009.

[20] James Welty, Charles Wicks, Robert Wilson, and Gregory Rorrer. *Fundamentals of Momentum, Heat, and Mass Transfer*. John Wiley and Sons, fourth edition, 2001.

[21] Pieter Wesseling. *Principles of Computational Fluid Dynamics*. Springer, 1991.

[22] Daniel Zwillinger. *CRC Standard Mathematical Tables and Formulae*. CRC Press, thirtieth edition, 1996.